Taylor & Francis
Taylor & Francis Group

Implementing the Theory of Sum Frequency Generation Vibrational Spectroscopy: A Tutorial Review

Alex G. Lambert and Paul B. Davies

Department of Chemistry, University of Cambridge, Cambridge, UK

David J. Neivandt

Department of Chemical and Biological Engineering,
University of Maine, Orono, Maine, USA

Abstract: The interfacial regions between bulk media, although often comprising only a fraction of the material present, are frequently the site of reactions and phenomena that dominate the macroscopic properties of the entire system. Spectroscopic investigations of such interfaces are often hampered by the lack of surface specificity of most available techniques. Sum frequency generation vibrational spectroscopy (SFS) is a non-linear optical technique which provides vibrational spectra of molecules solely at interfaces. The spectra may be analysed to provide the polar orientation, molecular conformation, and average tilt angle of the adsorbate to the surface normal. This article is aimed at newcomers to the field of SFS, and via a tutorial approach will present and develop the general sum frequency equations and then demonstrate how the fundamental theory elucidates the important experimental properties of SFS.

Keywords: Sum frequency generation vibrational spectroscopy, SFS, SFG, non-linear spectroscopy

INTRODUCTION

Sum frequency generation vibrational spectroscopy (SFS) is a surface-specific technique that provides vibrational spectra of molecules at interfaces (1, 2). SFS relies on the non-linear optical phenomenon of sum frequency generation (SFG). SFG occurs when two pulsed laser beams, one of fixed visible frequency, ω_{VIS}, and the other of tuneable infrared frequency, ω_{IR}, achieve spatial and temporal overlap at an interface. Light is emitted at the sum of the two incident frequencies, i.e., $\omega_{SF} = \omega_{VIS} + \omega_{IR}$. The intensity of the light is resonantly enhanced when the frequency of the tuneable infrared beam coincides with a vibrational mode of the molecules at the interface. By detecting the sum frequency (SF) light as a function of infrared frequency, a vibrational spectrum is obtained, which is up-shifted into the visible region of the electromagnetic spectrum.

The selection rules for SF activity differ from those for linear vibrational spectroscopy (such as those for infrared or Raman spectroscopies). Specifically, for a molecular vibrational mode (resonance) to be SF active, it must be in an asymmetric environment. The requirement for asymmetry must be satisfied on both macroscopic and molecular levels. On a macroscopic scale, an isotropic distribution of molecules in a bulk phase is centrosymmetric, i.e., it lacks asymmetry and is consequently SF inactive. Introduction of an interface into an isotropic bulk phase gives rise to a plane of asymmetry and the SF activity of exclusively the interfacial molecules. In addition, for the interfacial molecules to be SF active, they must have a net polar orientation. No SF emission arises from molecules arranged in an equal number of opposite orientations on a surface or from a completely disordered surface structure. SFS is consequently inherently interfacially specific and does not suffer from the difficulties associated with the signal from the surface being indistinguishable from that of the bulk medium, a drawback of linear vibrational spectroscopies (3). At a molecular level, the asymmetry condition for SF activity facilitates quantification of the degree of order (conformation) of the interfacial molecules. In addition, in systems containing a non-resonant signal, the spectral lineshape (phase) of an SF signal reports on the orientation of the species under investigation. Finally, as SFG is a coherent process and the light generated at the interface has a magnitude, direction, and phase which are specifically related to those of the incident laser beams, analysing spectra recorded with different incident beam polarisations allows the determination of the average tilt angle of the interfacial molecules (1, 2).

SFS is a comparatively new addition to the armoury for surface scientists. Although the theoretical basis for non-linear spectroscopy was set out by Bloembergen and Pershan (4) in 1962, the experimental observation of such phenomena had to wait for the advent of reliable high power pulsed lasers (5). The first SF spectra were recorded in the late 1980s by Shen (6, 7) and Harris (8). A rapidly expanding number of research groups currently use

SFS for a broad range of applications. Thus, SFS has been applied to investigations of bonding mechanisms, vibrational states, and orientations of species at the solid/vacuum interface including studies of CO (9–11), formic acid, (12) and cyclohexene (13) on catalytically important surfaces such as platinum, rhodium, and nickel. Atmospherically related problems have resulted in a number of studies (14) of the structure of surface water and ice (15), particularly in acidic (16) or strongly ionic (17) aqueous solutions. In more applied fields, SFS has been employed to probe chromatographic materials (18), combustion environments (19) and in tribology (20–22). Numerous studies have probed the orientation and conformation of surfactant species adsorbed at the solid/liquid (23, 24) and liquid/air interfaces (25, 26). Recently, SFS has been applied to the investigation of the behaviour of hydrocarbon chains under high applied pressures at the solid/solid interface (20–22). SF spectroscopy of polymeric species at interfaces was first reported in 2000 and is a rapidly expanding area of research (27, 28). Application of SFS to biological systems comprising lipid or protein is in its infancy but has great potential. Lipid conformations have recently been probed at water/oil (29, 30), solid/air (31), water/air (32), and solid/water interfaces (33). Similarly, in the last two years, the first SF studies of protein adsorption at a variety of interfaces has been reported. Specifically, SFS has been applied to studies of BSA, lysozyme, and fibrinogen conformational order at air (34, 35), silica (36, 37), polystyrene (36–38), and polymethylmethacrylate (39) surfaces.

Despite the broad use of SFS and the rapid expansion of the number of groups employing the technique, there exists no literature reviewing the theoretical background of the technique in a comprehensive manner that is accessible to the non-specialist. The present review builds on earlier expert reviews such as those of Shen (2) and Bain (1) with the aims of familiarizing the non-specialist, via a tutorial approach, with the origin of the phenomenon of SFG, developing the relevant fundamental theoretical relationships in a readily accessible manner, demonstrating how these theoretical relationships relate to the unique properties of SFS, and finally describing how the resulting spectra may be analysed to yield interface specific orientational and conformational information of molecular species. The present work is not intended as a review of the current developments and trends in SFS, such reviews are available in the existing literature (40–42). In what follows, an understanding of scalars, vectors, tensors, and their related nomenclature is assumed.

NON-LINEAR OPTICAL EFFECTS AND SUM FREQUENCY GENERATION

The electric field of a light wave propagating through a medium exerts a force on the valence electrons of the molecules comprising the

medium.[1] With ambient, low intensity and non-coherent light, this force is small and in an isotropic medium, the induced electric dipole, μ, is given by:

$$\boldsymbol{\mu} = \boldsymbol{\mu}_0 + \alpha\mathbf{E} \tag{1}$$

where μ_0 is the static (permanent) dipole of the material and α is the polarisability of the molecular electrons. In a condensed phase, the sum of the molecular electric dipoles gives rise to a dipole moment per unit volume, the bulk polarisation $\mathbf{P}$. Few materials have a static polarisation so considering only the polarisation induced by an oscillating electric field:

$$\mathbf{P} = \varepsilon_0\chi^{(1)}\mathbf{E} \tag{2}$$

where $\chi^{(1)}$ is the macroscopic average of α and is known as the first-order (or linear) susceptibility. ε_0 is the vacuum permittivity and gives $\mathbf{P}$ in SI units.[2] The induced dipole oscillates at the same frequency as the driving electric field and emits light at the frequency of the incident field. This produces linear optical properties such as reflection and refraction.

As the $\mathbf{E}$ field is increased the normally insignificant non-linearity increases and must be included in the description of the induced dipole by the incorporation of additional terms:

$$\boldsymbol{\mu} = \boldsymbol{\mu}_0 + \alpha\mathbf{E} + \beta\mathbf{E}^2 + \gamma\mathbf{E}^3 + \cdots \tag{3}$$

where β and γ are the first- and second-order hyperpolarisabilities, respectively. For bulk material (again assuming zero-static polarisation) the polarisation becomes:

$$\begin{aligned}
\mathbf{P} &= \varepsilon_0(\chi^{(1)}\mathbf{E} + \chi^{(2)}\mathbf{E}^2 + \chi^{(3)}\mathbf{E}^3 + \cdots) \\
&= \mathbf{P}^{(1)} + \mathbf{P}^{(2)} + \mathbf{P}^{(3)} + \cdots
\end{aligned} \tag{4}$$

where $\chi^{(2)}$ and $\chi^{(3)}$ are the second- and third-order non-linear susceptibilities, respectively, which are considerably smaller than $\chi^{(1)}$. Non-linear effects only become significant when the applied electromagnetic field is comparable with the field experienced by the electrons in a molecule. Fields of this magnitude are only normally achievable with pulsed lasers.

---

[1]Strictly speaking, the propagating wave exerts a force on both the valence electrons and the nucleus. However, within the Born–Oppenheimer approximation, the position of the nucleus is considered to be fixed as the relative displacement of the electrons is that much greater.

[2]Two systems of units are regularly used in electromagnetism: Standard International (SI) and Gaussian. The two systems differ in their definition of the electric permittivity of free space (ε_0) and the magnetic permeability of free space (μ_0). All the equations presented in this article use the SI units system, but may be converted to the Gaussian system by replacing ε_0 by $1/4\pi$.

It should be noted that in the theory developed here, the electric dipole approximation is used to describe the interaction of light with matter. Within this approximation, the effects of optical magnetic fields and of multipoles (e.g., quadrupoles) are neglected. In addition, it is assumed that the dipole induced within a molecule is solely due to the applied macroscopic field and that contributions from the dipolar fields of neighbouring induced dipoles may be ignored. The correction for this local field effect was first described by Lorentz (43) and its application to SF generation has been presented by Boyd (44) and discussed in greater detail by Casson (45) and Braun et al. (26). Local field effects should strictly be included for a rigorous description of induced non-linear polarisabilities. However, these effects are typically omitted from most theoretical SF studies (12) and are ignored here in favour of a succinct and accessible explanation of the origins of the SF signal.

The first successful non-linear optical experiment was reported by Franken and colleagues (46) in 1961 when they observed second harmonic generation (SHG) from a quartz crystal irradiated by a ruby laser. By expressing the frequency dependence of an incident electromagnetic field, it is possible to demonstrate the origin of SHG using Eq. (5), viz.,

$$\mathbf{E} = \mathbf{E}_1 \cos \omega t \tag{5}$$

where ω is the frequency of the incident light. The induced polarisation of Eq. (4) then becomes:

$$\mathbf{P} = \varepsilon_0(\chi^{(1)}(\mathbf{E}_1 \cos \omega t) + \chi^{(2)}(\mathbf{E}_1 \cos \omega t)^2 \\ + \chi^{(3)}(\mathbf{E}_1 \cos \omega t)^3 + \cdots) \tag{6}$$

which can be rewritten as:

$$\mathbf{P} = \varepsilon_0 \left(\chi^{(1)} \mathbf{E}_1 \cos \omega t + \frac{\chi^{(2)}}{2} \mathbf{E}_1^2 (1 + \cos 2\omega t) \\ + \frac{\chi^{(3)}}{4} \mathbf{E}_1^3 (3 \cos \omega t + \cos 3\omega t) + \cdots \right) \tag{7}$$

This equation shows that the induced polarisation, and hence the emitted light, contains terms that oscillate at twice (second harmonic generation), three times (third harmonic generation), etc., the frequency of the incident $\mathbf{E}$ field.

The origin of SFG may be demonstrated through an analogous argument, where the surface $\mathbf{E}$ field is expressed as the sum of two different oscillating incident fields, i.e., from two laser beams of frequency ω_1 and ω_2,

$$\mathbf{E} = \mathbf{E}_1 \cos \omega_1 t + \mathbf{E}_2 \cos \omega_2 t \tag{8}$$

Considering only the second-order (or quadratic) term of the polarisation, $\mathbf{P}^{(2)}$, and substituting for the combined $\mathbf{E}$ field gives:

$$\mathbf{P}^{(2)} = \varepsilon_0 \chi^{(2)} (\mathbf{E}_1 \cos \omega_1 t + \mathbf{E}_2 \cos \omega_2 t)^2$$

rearranging as before   (9)

$$\mathbf{E}_1^2 + \mathbf{E}_2^2$$

$$\mathbf{E}_1^2 \cos 2\omega_1 t + \mathbf{E}_2^2 \cos 2\omega_2 t \qquad \tfrac{1}{2}\mathbf{E}_1\mathbf{E}_2 \cos(\omega_1 - \omega_2)t \qquad \boxed{\tfrac{1}{2}\mathbf{E}_1\mathbf{E}_2 \cos(\omega_1 + \omega_2)t}$$

The two incident fields, therefore, give rise to a DC field (i.e., no frequency dependence or constant bias polarisation), SHG, for both the input frequencies, difference frequency generation (DFG), where light is emitted at the difference of the incident frequencies $\omega_1 - \omega_2$, and SFG, where light is emitted at the sum of the incident frequencies $\omega_1 + \omega_2$, ringed in Eq. (9). Although the simple electromagnetic approach adopted here is sufficient to demonstrate the origins of SFG, an exhaustive derivation is only obtainable through rigorous quantum mechanical calculations such as those presented by Shen (47) or Boyd (44).

   If the convention of not explicitly including the time dependence of the field is followed, the simplest description of the SF component of the second-order non-linear polarisation is:

$$\mathbf{P}^{(2)} = \varepsilon_0 \chi^{(2)} \mathbf{E}_1 \mathbf{E}_2 \qquad (10)$$

where $\chi^{(2)}$ (the second-order non-linear susceptibility) is a third-rank tensor describing the relationship between the two applied electric field vectors $\mathbf{E}_1$ and $\mathbf{E}_2$ and the resultant vector $\mathbf{P}^{(2)}$.

INTERACTION OF LASER LIGHT WITH A SURFACE

In this article, SFS is developed in the context of studying molecules present at a planar interface between two bulk phases. A co-ordinate system which follows the right-hand convention (i.e., rotation of a right-handed screw from x to y producing translation in the positive z direction) is adopted and is illustrated in Fig. 1. It should be noted that a variety of axis systems and beam geometries are in use in the literature (48, 49), and care must always be taken to relate equations to the specific field directions and axis system from which they were derived.

   When describing an electromagnetic wave incident on a planar surface, it is possible to resolve its associated $\mathbf{E}$ field into components that are polarised parallel (p) and perpendicular (s) to the plane of incidence (Fig. 2). Electromagnetic equations generally consider the s and p polarisations separately, because they behave differently at the interface. It may be seen that with the axis system of Fig. 1 and the beam geometries of Fig. 2, the $\mathbf{E}$ field produced at the surface
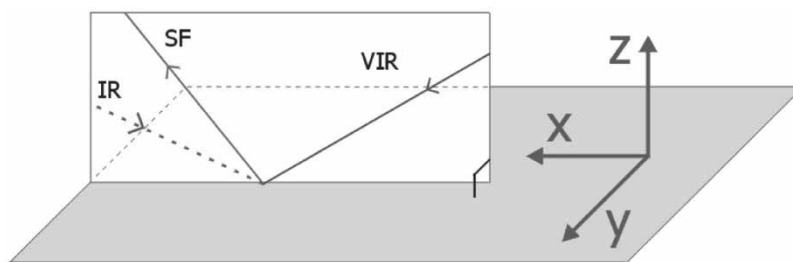
Figure 1. The surface fixed Cartesian co-ordinate system. The incident and emitted beams are shown for reference and propagate in the *xz* plane.
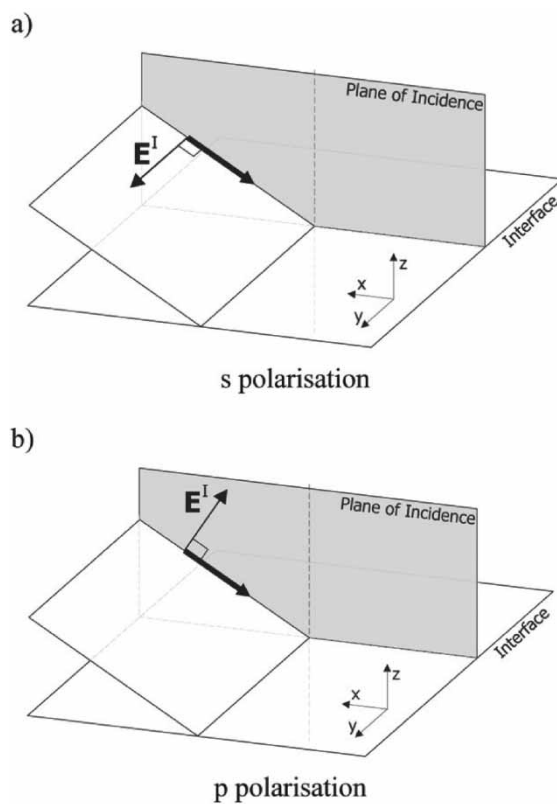

Figure 2. *s* and *p* polarized incident **E** fields. The superscript I indicates that the **E** fields shown originate from beams incident on the surface. The reflected and transmitted beams have been omitted for clarity. (a) *s* polarized light may be resolved into a single component perpendicular to the plane of incidence. (b) *p* polarized light may be resolved into two components parallel to the plane of incidence.

by s polarised light can be described by a surface bound electric field solely along the y axis, whereas the field established by incident p polarised light may be resolved into surface electric fields in both the x and z axes (Fig. 3).

The surface-based x, y, and z components of the incident light are given by Eqs. (11)–(13).

$$\mathbf{E}_x^\mathrm{I} = E_x^\mathrm{I} \cdot \hat{\mathbf{x}} \tag{11}$$

$$\mathbf{E}_y^\mathrm{I} = E_y^\mathrm{I} \cdot \hat{\mathbf{y}} \tag{12}$$

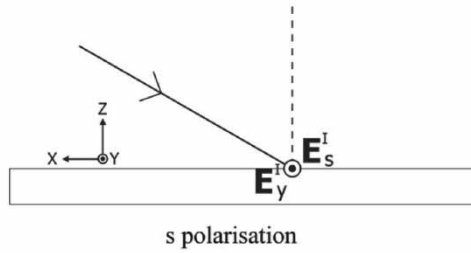$$\mathbf{E}_z^\mathrm{I} = E_z^\mathrm{I} \cdot \hat{\mathbf{z}} \tag{13}$$

where E_i^I is the magnitude of the resolved component along the i axis ($i = x$, y, or z) and $\hat{\mathbf{i}}$ is a unit vector along that axis. The relative magnitudes of the resolved components may be calculated trigonometrically (Fig. 3), viz.,

$$E_x^\mathrm{I} = \pm E_p^\mathrm{I} \cos \theta_\mathrm{I} \tag{14}$$

$$E_y^\mathrm{I} = E_s^\mathrm{I} \tag{15}$$

$$E_z^\mathrm{I} = E_p^\mathrm{I} \sin \theta_\mathrm{I} \tag{16}$$
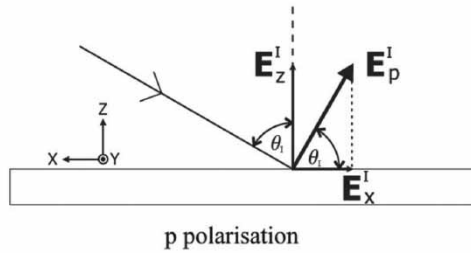

Figure 3. Resolving s and p polarised light at an interface. The superscript I indicates that an **E** field originates from a beam incident on the surface. θ_I is the angle of the incident beam to the surface normal. For clarity, the reflected and transmitted beams are not shown.

where the positive sign in Eq. (14) is employed if the incident beam is propagating in the positive x direction, whereas the negative sign is employed if the incident beam propagates in the negative x direction.

The extent to which a beam is reflected or transmitted at an interface can be determined using Fresnel coefficients and equations (50). For a diamagnetic material, the Fresnel equations involve the angle of incidence and transmission of a beam relative to the surface normal (θ_I and θ_T, respectively) and the refractive indices of the two media (n_I and n_T, respectively) (Fig. 4). The Fresnel amplitude coefficients for reflection and transmission in the s and p polarisations are given by (50):

$$r_s \equiv \left(\frac{E_s^R}{E_s^I}\right) = \frac{n_I \cos\theta_I - n_T \cos\theta_T}{n_I \cos\theta_I + n_T \cos\theta_T} \tag{17}$$

$$r_p \equiv \left(\frac{E_p^R}{E_p^I}\right) = \frac{n_T \cos\theta_I - n_I \cos\theta_T}{n_I \cos\theta_T + n_T \cos\theta_I} \tag{18}$$

a)

S polarisation

b)

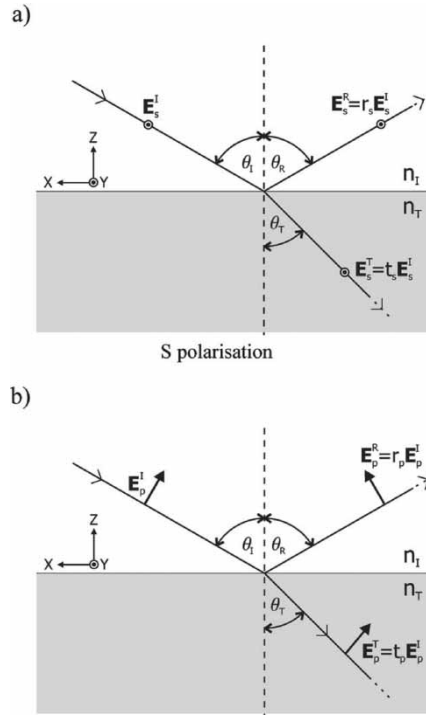*Figure 4.* Incident, reflected, and transmitted beams for s and p polarised light. E^I, E^R, and E^T are the incident, reflected, and transmitted **E** field vectors, respectively. r and t are the Fresnel amplitude coefficients for reflection and transmission. n_I and n_T are the refractive indices of the incident and transmitting media.

$$t_s \equiv \left(\frac{E_s^{\mathrm{T}}}{E_s^{\mathrm{I}}}\right) = \frac{2n_{\mathrm{I}} \cos \theta_{\mathrm{I}}}{n_{\mathrm{I}} \cos \theta_{\mathrm{I}} + n_{\mathrm{T}} \cos \theta_{\mathrm{T}}} \tag{19}$$

$$t_p \equiv \left(\frac{E_p^{\mathrm{T}}}{E_p^{\mathrm{I}}}\right) = \frac{2n_{\mathrm{I}} \cos \theta_{\mathrm{I}}}{n_{\mathrm{I}} \cos \theta_{\mathrm{T}} + n_{\mathrm{T}} \cos \theta_{\mathrm{I}}} \tag{20}$$

The total electric field present at the interface is the sum of the fields of the incident and reflected beams. Therefore, the magnitudes of the interfacial electric field components are given by

$$E_x = E_x^{\mathrm{I}} + E_x^{\mathrm{R}} = E_x^{\mathrm{I}} + r_p E_x^{\mathrm{I}} = \mp \left(E_p^{\mathrm{I}} \cos \theta_{\mathrm{I}} - r_p E_p^{\mathrm{I}} \cos \theta_{\mathrm{I}} \right)$$

$$= \mp E_p^{\mathrm{I}} \cos \theta_{\mathrm{I}} (1 - r_p) \tag{21}$$

$$E_y = E_y^{\mathrm{I}} + E_y^{\mathrm{R}} = E_y^{\mathrm{I}} + r_s E_y^{\mathrm{I}} = E_s^{\mathrm{I}} + r_s E_s^{\mathrm{I}} = E_s^{\mathrm{I}} (1 + r_s) \tag{22}$$

$$E_z = E_z^{\mathrm{I}} + E_z^{\mathrm{R}} = E_z^{\mathrm{I}} + r_p E_z^{\mathrm{I}} = E_p^{\mathrm{I}} \sin \theta_{\mathrm{I}} + r_p E_p^{\mathrm{I}} \sin \theta_{\mathrm{I}}$$

$$= E_p^{\mathrm{I}} \sin \theta_{\mathrm{I}} (1 + r_p) \tag{23}$$

The beam directions depicted in Fig. 4, corresponding to the IR beam in the SF experiment depicted in Fig. 1, result in field directions which are negative for E_x^{I} and positive for E_x^{R}, thereby making Eq. (21) negative. However, if an incident beam propagates in the opposite direction, such as the visible beam of Fig. 1, E_x^{I} is positive and E_x^{R} is negative, thereby making Eq. (21) positive.

THE SUM FREQUENCY EQUATION

Sum frequency spectroscopy is generally used to probe vibrational resonances of molecules adsorbed at interfaces and, consequently, one of the incident beams is selected to be tuneable in the infrared frequency range. However, the accurate detection of low intensity light is experimentally easiest in the visible region of the electromagnetic spectrum and, therefore, the second incident beam is chosen to be at a fixed visible (or near-infrared) frequency. From Eq. (9), it follows that the frequency of the emitted SF signal is simply the sum of the tuneable infrared and the fixed visible beam frequencies:

$$\omega_{\mathrm{SF}} = \omega_{\mathrm{IR}} + \omega_{\mathrm{VIS}} \tag{24}$$

Equation (10) can be rewritten as:

$$\mathbf{P}_{\mathrm{SF}}^{(2)} = \varepsilon_0 \chi^{(2)} \mathbf{E}_{\mathrm{VIS}} \mathbf{E}_{\mathrm{IR}} \tag{25}$$

In order to achieve SF generation, spatial and temporal overlap of the infrared and visible beams on the surface is essential. A coherent SF signal is subsequently generated at an angle to the surface normal of θ_{SF}, which can be calculated using the conservation of momentum of all three beams parallel

to the interface (known as the phase-matching condition), as follows:

$$n_{SF}\omega_{SF} \sin \theta_{SF} = n_{VIS}\omega_{VIS} \sin \theta_{VIS} \pm n_{IR}\omega_{IR} \sin \theta_{IR} \qquad (26)$$

or

$$n_{SF}k_{SF} \sin \theta_{SF} = n_{VIS}k_{VIS} \sin \theta_{VIS} \pm n_{IR}k_{IR} \sin \theta_{IR} \qquad (27)$$

where n is the refractive index of the medium through which the relevant beam propagates, ω is the frequency, θ is the angle to the surface normal of each beam, and k is equal to ω/c, where c is the speed of light. Equation (27) is commonly used in preference to Eq. (26), as the unit of k is a wavenumber. The positive sign refers to co-propagating beams (visible and infrared beams arriving from the same x direction) and the negative sign to counter-propagating beams (visible and infrared beams arrive from opposite x directions, as in Fig. 5). SF light is both reflected from and transmitted into the surface. The more accessible of these two beams is usually detected.

Induced Polarisation in Surface Bound Co-ordinates

Although Eq. (25) fully describes SF generation from a surface, it does so in a manner which is independent of a co-ordinate system. To develop and interpret Eq. (25), it is necessary to define its relationship with the surface **E** fields and the incident and generated beams using the surface bound Cartesian co-ordinate system introduced earlier. As $\chi^{(2)}$ is a third-rank tensor, it has 27 different components in Cartesian space, each component corresponding to a different combination of applied vectors. Equation (25) may consequently be rewritten in terms of the Cartesian axis system as in Eq. (28), where a single representative
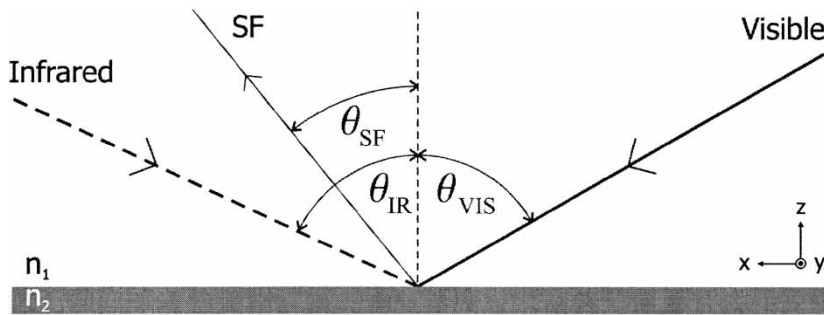

Figure 5. The counter-propagating SF beam geometry. In an SF experiment, both the infrared and the SF beams are invisible to the naked eye (the SF beam is invisible due to its low intensity). The reflected infrared and visible beams have been omitted from the diagram for clarity. Further, SF is also generated into the substrate (not shown) at an angle from the surface normal calculated using n_2 instead of n_1 for n_{SF} in Eqs. (26) and (27).

combination of applied vectors is employed by considering purely the polarisation induced in the i direction by the **E** fields in the j and k axes:

$$\mathbf{P}^{(2)}_{i,\mathrm{SF}} = \varepsilon_0 \chi^{(2)}_{ijk} \mathbf{E}_{j,\mathrm{VIS}} \mathbf{E}_{k,\mathrm{IR}} \tag{28}$$

However, Eq. (28) is only 1/27th of the description of the SF signal from a surface (e.g., $\mathbf{P}_{x,\mathrm{SF}}$ created by $\mathbf{E}_{y,\mathrm{VIS}}$, $\mathbf{E}_{z,\mathrm{IR}}$, and $\chi^{(2)}_{xyz}$, or $\mathbf{P}_{z,\mathrm{SF}}$ created by $\mathbf{E}_{z,\mathrm{VIS}}$, $\mathbf{E}_{z,\mathrm{IR}}$, and $\chi^{(2)}_{zzz}$). A complete description of SFG from the surface must, therefore, consider all 27 possible tensor components, viz.,

$$\mathbf{P}^{(2)}_{\mathrm{SF}} = \sum_i^{x,y,z} \mathbf{P}^{(2)}_{i,\mathrm{SF}} = \varepsilon_0 \sum_i^{x,y,z} \sum_j^{x,y,z} \sum_k^{x,y,z} \chi^{(2)}_{ijk} \mathbf{E}_{j,\mathrm{VIS}} \mathbf{E}_{k,\mathrm{IR}} \tag{29}$$

For simplicity, further development of the SF equation will consider only the single combination of representative components given by Eq. (28). Nevertheless, the total SF signal can only be calculated from a summation over all components.

K Factors: Surface E Fields from Incident E Fields

Equation (28) relates specifically to the electric field vectors at the surface, not to those propagating through space. Using the Fresnel equations [Eqs. (17), (18), and (21)–(23)], the surface **E** fields generated by the incident **E** fields may be calculated in terms of s and p polarisations, as follows:

$$\mathbf{E}_x = E_x \hat{\mathbf{x}} = \mp E_p^{\mathrm{I}} \cos\theta_{\mathrm{I}}(1 - r_p)\hat{\mathbf{x}} = K_x E_p^{\mathrm{I}}\hat{\mathbf{x}} \tag{30}$$

$$\mathbf{E}_y = E_y \hat{\mathbf{y}} = (1 + r_s)E_s^{\mathrm{I}}\hat{\mathbf{y}} = K_y E_s^{\mathrm{I}}\hat{\mathbf{y}} \tag{31}$$

$$\mathbf{E}_z = E_z \hat{\mathbf{z}} = E_p^{\mathrm{I}} \sin\theta_{\mathrm{I}}(1 + r_p)\hat{\mathbf{z}} = K_z E_p^{\mathrm{I}}\hat{\mathbf{z}} \tag{32}$$

where

$$K_x = \mp \cos\theta_{\mathrm{I}}(1 - r_p) = \mp \cos\theta_{\mathrm{I}}\left(1 - \frac{n_{\mathrm{T}}\cos\theta_{\mathrm{I}} - n_{\mathrm{I}}\cos\theta_{\mathrm{T}}}{n_{\mathrm{I}}\cos\theta_{\mathrm{T}} + n_{\mathrm{T}}\cos\theta_{\mathrm{I}}}\right)$$

$$= \mp \frac{2n_{\mathrm{I}}\cos\theta_{\mathrm{I}}\cos\theta_{\mathrm{T}}}{n_{\mathrm{I}}\cos\theta_{\mathrm{T}} + n_{\mathrm{T}}\cos\theta_{\mathrm{I}}} \tag{33}$$

For the counter-propagating beam geometry depicted in Fig. 5, K_x is positive for the visible beam and negative for the infrared beam. Similarly, the equations for K_y and K_z are given by:

$$K_y = (1 + r_s) = \frac{2n_{\mathrm{I}}\cos\theta_{\mathrm{I}}}{n_{\mathrm{I}}\cos\theta_{\mathrm{I}} + n_{\mathrm{T}}\cos\theta_{\mathrm{T}}} \tag{34}$$

$$K_z = \sin\theta_{\mathrm{I}}(1 + r_p) = \frac{2n_{\mathrm{I}}\sin\theta_{\mathrm{I}}\cos\theta_{\mathrm{I}}}{n_{\mathrm{I}}\cos\theta_{\mathrm{T}} + n_{\mathrm{T}}\cos\theta_{\mathrm{I}}} \tag{35}$$

Using Eqs. (30)–(32), the generic SF polarisation equation [Eq. (28)] may now be expressed in terms of the magnitude of the incident beams, viz.,

$$\mathbf{P}^{(2)}_{i,\text{SF}} = \varepsilon_0 \chi^{(2)}_{ijk} \hat{\mathbf{j}} K_j E^{\text{I}}_{p/s,\text{VIS}} \hat{\mathbf{k}} K_k E^{\text{I}}_{p/s,\text{IR}} \tag{36}$$

By convention, the unit vectors are implicitly included to give

$$\mathbf{P}^{(2)}_{i,\text{SF}} = \varepsilon_0 \chi^{(2)}_{ijk} K_j E^{\text{I}}_{p/s,\text{VIS}} K_k E^{\text{I}}_{p/s,\text{IR}} \tag{37}$$

L Factors: Generating SF E Fields from Induced Polarisations

The non-linear induced polarisation at the interface, $\mathbf{P}^{(2)}_{i,\text{SF}}$ [Eq. (37)] generates a surface bound SF electric field. The resulting SF light is emitted from the interface at a specific angle due to phase matching [Eqs. (26) and (27)]. To relate the induced polarisation to the emitted SF **E** field and to take into account phase matching, non-linear SF Fresnel factors, or *L* factors are employed.

$$\mathbf{E}_{i,\text{SF}} = L_i \mathbf{P}^{(2)}_{i,\text{SF}} \tag{38}$$

where $i = x$, y, or z. Six *L*-factors exist, three for SF emission in the "rare" (reflection) medium (L_i^{R}) and three for SF emission into the "dense" (transmission) medium (L_i^{T}). *L*-factors were originally derived by Heinz (48) and have subsequently been published by Hirose et al. (49). The derivation combines the continuity of **E** fields across an interface with the phase matching restrictions on the angle of SF emission. Both authors use a different axis system from that employed here and, consequently, sign changes have been included in the following equations where necessary.

$$L_x^{\text{R}} = -\frac{i\omega_{\text{SF}}}{c\varepsilon_0} \frac{\cos\theta_{\text{SF}}^{\text{T}}}{n_{\text{T}}\cos\theta_{\text{SF}}^{\text{I}} + n_{\text{I}}\cos\theta_{\text{SF}}^{\text{T}}} \tag{39}$$

$$L_y^{\text{R}} = \frac{i\omega_{\text{SF}}}{c\varepsilon_0} \frac{1}{n_{\text{I}}\cos\theta_{\text{SF}}^{\text{I}} + n_{\text{T}}\cos\theta_{\text{SF}}^{\text{T}}} \tag{40}$$

$$L_z^{\text{R}} = \frac{i\omega_{\text{SF}}}{c\varepsilon_0} \frac{(n_{\text{T}}/n_{\text{layer}})^2 \sin\theta_{\text{SF}}^{\text{T}}}{n_{\text{I}}\cos\theta_{\text{SF}}^{\text{T}} + n_{\text{T}}\cos\theta_{\text{SF}}^{\text{I}}} \tag{41}$$

$$L_x^{\text{T}} = \frac{i\omega_{\text{SF}}}{c\varepsilon_0} \frac{\cos\theta_{\text{SF}}^{\text{I}}}{n_{\text{T}}\cos\theta_{\text{SF}}^{\text{I}} + n_{\text{I}}\cos\theta_{\text{SF}}^{\text{T}}} \tag{42}$$

$$L_y^{\text{T}} = \frac{i\omega_{\text{SF}}}{c\varepsilon_0} \frac{1}{n_{\text{I}}\cos\theta_{\text{SF}}^{\text{I}} + n_{\text{T}}\cos\theta_{\text{SF}}^{\text{T}}} \tag{43}$$

$$L_z^{\text{T}} = \frac{i\omega_{\text{SF}}}{c\varepsilon_0} \frac{(n_{\text{I}}/n_{\text{layer}})^2 \sin\theta_{\text{SF}}^{\text{I}}}{n_{\text{I}}\cos\theta_{\text{SF}}^{\text{T}} + n_{\text{T}}\cos\theta_{\text{SF}}^{\text{I}}} \tag{44}$$

where ω_{SF}, c, and ε_0 are present to provide the SF equation with the correct units and i introduces a constant phase term. The trigonometric factors are amplitude coefficients in an identical manner to those found in linear Fresnel factors and n_{layer} is the refractive index of an adsorbed layer at the interface of the two bulk phases (not necessarily identical to the refractive index of the bulk material). θ_{SF}^I and θ_{SF}^T are the angles of SF emission into the incident and the transmitting media, respectively.

The intensity of the s or p polarised SF light emitted from the surface and subsequently detected can be expressed as the sum of the squares of the magnitudes of the component SF **E** fields, viz.,

$$I_{p,SF} \propto \left|\mathbf{E}_{x,SF}\right|^2 + \left|\mathbf{E}_{z,SF}\right|^2 \tag{45}$$

$$\propto \left|L_x\mathbf{P}_{x,SF}^{(2)}\right|^2 + \left|L_z\mathbf{P}_{z,SF}^{(2)}\right|^2 \tag{46}$$

$$\propto \left|L_x \sum_j^{x,y,z} \sum_k^{x,y,z} \varepsilon_0\chi_{xjk}^{(2)}K_jE_{pVIS}^I K_kE_{pIR}^I\right|^2$$

$$+ \left|L_z \sum_j^{x,y,z} \sum_k^{x,y,z} \varepsilon_0\chi_{zjk}^{(2)}K_jE_{pVIS}^I K_kE_{pIR}^I\right|^2 \tag{47}$$

$$I_{s,SF} \propto \left|\mathbf{E}_{y,SF}^I\right|^2 \tag{48}$$

$$\propto \left|L_y\mathbf{P}_{y,SF}^{(2)}\right|^2 \tag{49}$$

$$\propto \left|L_y \sum_j^{x,y,z} \sum_k^{x,y,z} \varepsilon_0\chi_{yjk}^{(2)}K_jE_{pVIS}^I K_kE_{pIR}^I\right|^2 \tag{50}$$

Second-Order Non-linear Susceptibility, $\chi^{(2)}$

Although Eqs. (47) and (50) contain numerous terms, only the second-order non-linear susceptibility, $\chi^{(2)}$, changes significantly with infrared wavenumber and it is, therefore, solely responsible for the vibrational information obtained from a sum frequency spectrum. $\chi^{(2)}$ is the macroscopic average of the molecular hyperpolarisabilities, β, of the molecules adsorbed at the interface. As the frequency of the infrared laser beam is tuned through a resonance, it is the values of the β components, and hence $\chi^{(2)}$, that increase and produce a change in the SF signal intensity, which is observed at the detector.

A description of the complete mathematical relationship between β and $\chi^{(2)}$ is given elsewhere (e.g., Ref. (51)); however, for a general understanding of SFG, this level of complexity is not required. Consequently, an overview describing

the basis of the progression from β to $\chi^{(2)}$, including the fundamental expressions that generate resonant SF enhancement, is given in the following text.

In contrast to the surface bound Cartesian axis system (x, y, z) used to date, it is more convenient when working at a molecular level to employ a molecular bound co-ordinate system (a, b, c). Generic indices (α, β, γ) are used, taking values of a, b, or c in an analogous manner to that in which (i, j, k) are used in the surface axis system for x, y, or z. In a comparable manner to $\chi^{(2)}$, $\beta_{\alpha\beta\gamma}$ has a total of 27 possible components that describe the non-linear response of the molecule to all incident and emitted **E** field polarisation combinations. Symmetry considerations, however, often reduce the number of non-zero $\beta_{\alpha\beta\gamma}$ components considerably (52). Each non-zero $\beta_{\alpha\beta\gamma}$ is associated with a particular molecular vibration. The sum of all the non-zero $\beta_{\alpha\beta\gamma}$ components describes the complete response of the molecule to the visible and infrared **E** fields.

The symmetry axis of a molecule adsorbed at an interface often lies at an angle to the surface normal, so that molecular and surface-bound co-ordinate systems rarely coincide. Experimentally, the **E** fields applied to a surface are always evaluated relative to the surface bound rather than molecular bound co-ordinate system. Consequently, although an **E** field in the surface co-ordinate system may be in a specific polarised direction $(x, y, \text{or } z)$, relative to the molecular-based system, it could be resolved into components in all three molecular directions $(a, b, \text{and } c)$. To describe the relationship between the two co-ordinate systems, three Euler angles (θ, ϕ, ψ) are required (51). Three rotation matrices (one for each of the Euler angles) are used to convert between the two systems. Although the full process is described in Ref. (51), a simplified example considering only one Euler angle and one matrix is provided in Fig. 6 and discussed as follows to demonstrate the concept.

Figure 6(a) represents a molecule adsorbed with its symmetry axis perpendicular to the surface, as such the surface and molecular-bound axis systems are aligned. Consequently, the molecule experiences $\mathbf{E}_x$ and $\mathbf{E}_z$ in purely the a and c axes, respectively, i.e.,

$$\mathbf{E}_x = \mathbf{E}_a \quad \mathbf{E}_y = \mathbf{E}_b \quad \mathbf{E}_z = \mathbf{E}_c \tag{51}$$

Conversely, Fig. 6(b) depicts a molecule adsorbed at an angle θ to the surface normal. The two co-ordinate systems are no longer aligned but are related by a simple rotation matrix with a single Euler angle of θ, viz.,

$$\mathbf{E}_x = \mathbf{E}_a \cos\theta - \mathbf{E}_c \sin\theta \tag{52}$$

$$\mathbf{E}_y = \mathbf{E}_b \tag{53}$$

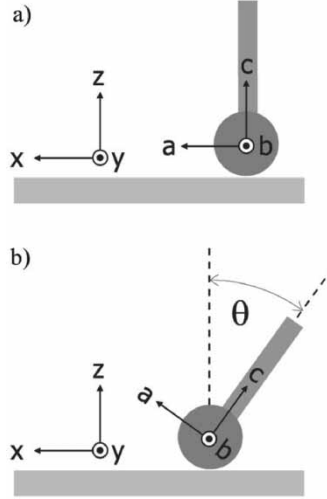$$\mathbf{E}_z = \mathbf{E}_a \sin\theta + \mathbf{E}_c \cos\theta \tag{54}$$

Figure 6.   (a) Schematic representation of a molecule adsorbed perpendicular to a surface. The surface and molecular bound axis systems are aligned and the molecule experiences $\mathbf{E}_x$ and $\mathbf{E}_z$ in purely the a and c axes, respectively. (b) A molecule adsorbed at an angle θ to the surface normal. The surface and molecular bound axis systems are related by a simple rotation matrix with a Euler angle of θ.

or

$$
\begin{pmatrix} \mathbf{E}_x \\ \mathbf{E}_y \\ \mathbf{E}_z \end{pmatrix} = \begin{pmatrix} \cos\theta & 0 & -\sin\theta \\ 0 & 1 & 0 \\ \sin\theta & 0 & \cos\theta \end{pmatrix} \begin{pmatrix} \mathbf{E}_a \\ \mathbf{E}_b \\ \mathbf{E}_c \end{pmatrix} \tag{55}
$$

Macroscopic Averaging

$\chi_{ijk}^{(2)}$ is a macroscopic average of $\beta_{\alpha\beta\gamma}$ and is, therefore, a sum over all the adsorbed molecules in a given volume. The sum may be written as follows:

$$
\chi_{ijk}^{(2)} = \frac{N}{\varepsilon_0} \sum_{\alpha\beta\gamma} \langle R(\psi)R(\theta)R(\varphi)\beta_{\alpha\beta\gamma} \rangle \tag{56}
$$

where $R(\psi)R(\theta)R(\varphi)$ is the product of three rotation matrices using all three Euler angles to convert from the molecular to surface co-ordinate systems. The $\langle \rangle$ brackets indicate the orientational averages and N is the number of molecules per unit volume.

A quantum mechanical expression for $\beta_{\alpha\beta\gamma}$ may be derived using perturbation theory (52). A simplification of the general equation is presented here

that is applicable when ω_{IR} is near a vibrational resonance and ω_{VIS} is removed from the frequency of electronic transitions:

$$\beta_{\alpha\beta\gamma} = \frac{1}{2\hbar} \frac{M_{\alpha\beta}A_\gamma}{(\omega_v - \omega_{IR} - i\Gamma)} \tag{57}$$

where ω_{IR} is the frequency of the tuneable infrared beam, ω_v is the frequency of the vibrational resonance, and Γ^{-1} is the relaxation time of the vibrationally excited state involved in the resonance. $M_{\alpha\beta}$ and A_γ are the Raman and infrared transition moments, respectively. Equation (57) reveals the origin of an SF selection rule that a resonance must be both Raman and infrared active. $M_{\alpha\beta}$ and A_γ are defined in Eqs. (58) and (59), respectively.

$$M_{\alpha\beta} = \sum_s \left[\frac{\langle g|\mu_\alpha|s\rangle\langle s|\mu_\beta|v\rangle}{\hbar(\omega_{SF} - \omega_{sg})} - \frac{\langle g|\mu_\beta|s\rangle\langle s|\mu_\alpha|v\rangle}{\hbar(\omega_{VIS} + \omega_{sg})} \right] \tag{58}$$

$$A_\gamma = \langle v|\mu_\gamma|g\rangle \tag{59}$$

where μ is the electric dipole operator, $|g\rangle$ is the ground state, $|v\rangle$ is the excited vibrational state, and $|s\rangle$ is any other state. A diagrammatic representation of the resonance enhancement process is given in Fig. 7.

The change that occurs in $\chi^{(2)}_{ijk}$ on resonance becomes clear by substituting the frequency dependent terms of $\beta_{\alpha\beta\gamma}$ in Eq. (57) into the macroscopic $\chi^{(2)}_{ijk}$

OFF RESONANCE

The incident beam energies do not correspond to any molecular energy levels. SFG is minimal

ON RESONANCE

The energy of the infrared radiation now matches a molecular vibration and the SF process is resonantly enhanced
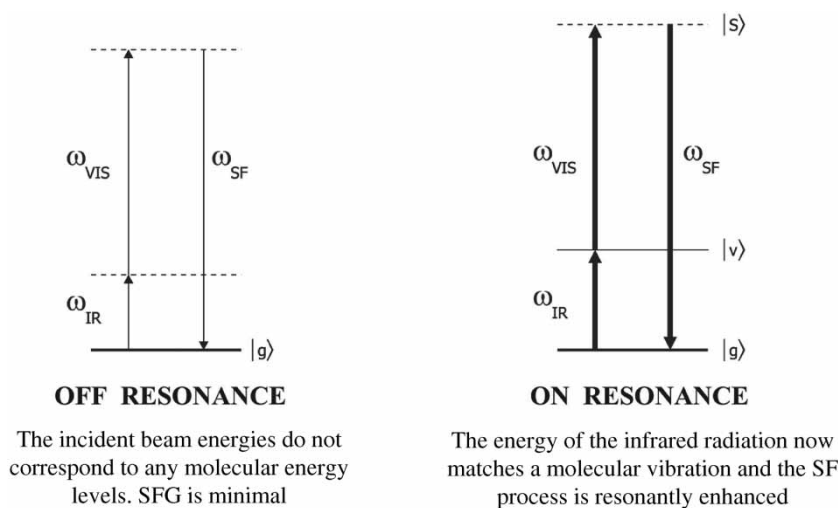
Figure 7. Energy level schemes for one of the eight Liouville paths responsible for SFG (47). The SF process is shown on and off resonance.

equation [Eq. (56)]. A common expression for $\chi_{ijk}^{(2)}$ is, therefore, given by

$$\chi_{ijk}^{(2)} = \frac{N \sum\limits_{\alpha\beta\gamma} \langle R(\psi)R(\theta)R(\phi)\beta_{\alpha\beta\gamma} \rangle}{\varepsilon_0(\omega_v - \omega_{IR} - i\Gamma)} \tag{60}$$

When the infrared frequency (ω_{IR}) coincides with the frequency of a vibrational mode (ω_v) of the interfacial molecules, then $\omega_v - \omega_{IR}$ goes to 0 and the magnitude of $\chi_{ijk}^{(2)}$ increases. An increase in SFG will, therefore, occur at the resonant frequency. Detecting the SF light as a function of IR frequency subsequently yields a vibrational spectrum of the adsorbed molecules.

EXPERIMENTAL IMPLICATIONS OF THE SUM FREQUENCY EQUATION

Surface Specificity

Although the non-linear susceptibility term $\chi_{ijk}^{(2)}$ has a maximum of 27 components, the number of unique contributing, or non-zero, components is less due to symmetry constraints. In a centrosymmetric environment, all directions are equivalent and the value of $\chi_{ijk}^{(2)}$ for two opposing directions must, therefore, be identical, viz.,

$$\chi_{ijk}^{(2)} = \chi_{-i-j-k}^{(2)} \tag{61}$$

However, as $\chi_{ijk}^{(2)}$ is a third rank tensor, a change in the sign of the three subscripts is simply equivalent to reversing the axis system, and the physical phenomenon $\chi_{ijk}^{(2)}$ describes must, therefore, reverse sign, i.e.,

$$\chi_{ijk}^{(2)} = -\chi_{-i-j-k}^{(2)} \tag{62}$$

To satisfy both Eqs. (61) and (62), $\chi_{ijk}^{(2)}$ must equal 0, with the result that in a centrosymmetric medium SFG is forbidden. Although the majority of bulk phases are centrosymmetric, the boundary between two materials is inherently non-centrosymmetric and, therefore, SF active. The planar surfaces considered here are isotropic, symmetric about the surface normal, and thus contain a C_∞ rotation axis, as depicted in Fig. 8.

With a C_∞ surface, $z \neq -z$ but $x \equiv -x$ and $y \equiv -y$. A similar argument to that outlined earlier can now be applied. As $x \equiv -x$ and $y \equiv -y$, a non-zero contributing $\chi_{ijk}^{(2)}$ on a C_∞ surface would not change sign if the x or y axis is reversed, as essentially no change has actually taken place. However, the fundamental tensor rule shown in Eq. (62) still applies; if the direction of any individual axis is reversed, the directionally dependent value of the $\chi_{ijk}^{(2)}$ must change sign. Only a limited number of vector combinations can satisfy
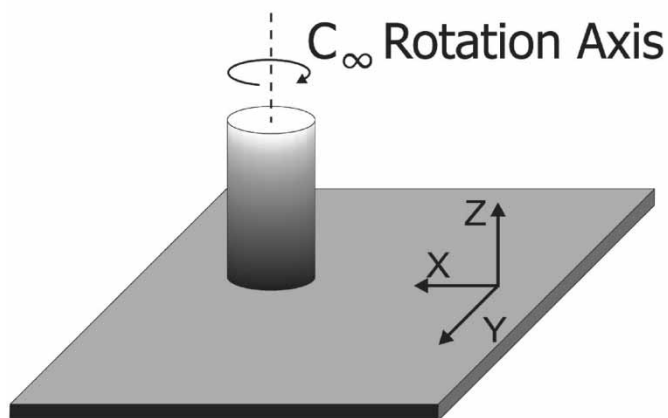
Figure 8. A planar surface symmetric about the surface normal.

both these rules, and the methodology used to identify the contributing combinations is given for a number of examples as shown in Table 1.

Table 1 may be summarised by the statement that apart from zzz, only quadratic terms in either *x* or *y* contribute. The complete series of eliminations is, therefore, given by

~~xxx~~	~~xyx~~	xzx	~~yxx~~	~~yyx~~	~~yzx~~	zxx	~~zyx~~	~~zzx~~
~~xxy~~	~~xyy~~	~~xzy~~	~~yxy~~	~~yyy~~	yzy	~~zxy~~	zyy	~~zzy~~
xxz	~~xyz~~	~~xzz~~	~~yxz~~	yyz	~~yzz~~	~~zxz~~	~~zyz~~	zzz

Because the *x* and *y* axes are equivalent for an isotropic surface, the overall result is that a surface with C_∞ symmetry has only four independent non-zero $\chi_{ijk}^{(2)}$ components that can potentially generate a SF signal:

$$\chi_{zxx}^{(2)} \ (\equiv\chi_{zyy}^{(2)}) \quad \chi_{xzx}^{(2)} \ (\equiv\chi_{yzy}^{(2)}) \quad \chi_{xxz}^{(2)} \ (\equiv\chi_{yyz}^{(2)}) \quad \chi_{zzz}^{(2)}$$

Resonant and Non-resonant Susceptibilities

The derivations presented so far are appropriate for a system containing interfacial molecules adsorbed on a surface which is SF inactive. However, if the underlying substrate is SF active, an additional susceptibility to describe the behaviour of the substrate is required. The substrate susceptibility is termed as $\chi_{NR}^{(2)}$, where the NR subscript refers to its non-resonant nature. Because the susceptibility used so far ($\chi^{(2)}$) is related solely to the resonant behaviour of the interfacial molecules, it is renamed $\chi_R^{(2)}$. A generic

Table 1.   Deducing the contributing $\chi_{ijk}^{(2)}$s for an isotropic surface

$\chi_{ijk}^{(2)}$	Operation	Result
zxx	Reversing the x axis produces $z-x-x$. $\chi_{z-x-x}^{(2)}\equiv$ $-\chi_{zx-x}^{(2)}\equiv\chi_{zxx}^{(2)}$. There is no overall change in the sign of $\chi_{zxx}^{(2)}$ with reversal of axis, both rules are satisfied. Substituting x for y and reversing the y axis has the same effect.	Contributes
zzz	Reversing either the x or y axis has no effect.	Contributes
zzx	Reversing the x axis produces $zz-x$, $\chi_{zz-x}^{(2)}\equiv-\chi_{zzx}^{(2)}$. $\chi_{zzx}^{(2)}$ changes sign with reversal of axis, both rules are not satisfied unless equal to 0.	Zero
yyy	Reversing the y axis produces $-y-y-y$. $\chi_{-y-y-y}^{(2)}\equiv-\chi_{y-y-y}^{(2)}\equiv\chi_{yy-y}^{(2)}\equiv-\chi_{yyy}^{(2)}$. Sign change occurs, both rules are not satisfied.	Zero

description of the response of the interface to applied **E** field vectors is, therefore, given by

$$\chi^{(2)} = \chi_R^{(2)} + \chi_{NR}^{(2)} \tag{63}$$

For dielectric materials, $\chi_{NR}^{(2)}$ is typically very small unless ω matches a molecular transition, which is uncommon. Conversely, for metal surfaces, $\chi_{NR}^{(2)}$ is of a significant magnitude due to surface plasmon resonance, and a considerable SF signal is generated, which is largely invariant with frequency. As SFG at an interface is a combination of both resonant and non-resonant signals, an understanding of the complex nature of both $\chi_R^{(2)}$ and $\chi_{NR}^{(2)}$ is necessary.

Resonant Susceptibility, $\chi_{R,ijk}^{(2)}$

The frequency dependent term in a single non-zero component of $\chi_R^{(2)}$ [Eq. (60)] is given by:

$$\frac{1}{(\omega_v - \omega_{IR} - i\Gamma)} \tag{64}$$

The real and imaginary components of the frequency dependency of $\chi_{R,\,ijk}^{(2)}$ may be separated by multiplying Eq. (64) by its complex conjugate, viz.,

$$\frac{1}{\omega_v - \omega_{IR} - i\Gamma} \cdot \frac{\omega_v - \omega_{IR} + i\Gamma}{\omega_v - \omega_{IR} + i\Gamma} = \frac{\omega_v - \omega_{IR} + i\Gamma}{(\omega_v - \omega_{IR})^2 + \Gamma^2}$$

$$= \frac{\omega_v - \omega_{IR}}{(\omega_v - \omega_{IR})^2 + \Gamma^2} + i\frac{\Gamma}{(\omega_v - \omega_{IR})^2 + \Gamma^2} \tag{65}$$

The real and imaginary components of $\chi_{R,ijk}^{(2)}$ are plotted in Fig. 9 as a function of infrared wavenumber in a region containing an arbitrary resonance at $2900\,\text{cm}^{-1}$.

$\chi_{R,ijk}^{(2)}$ can also be expressed in polar co-ordinates:

$$\chi_{R,ijk}^{(2)} = \left|\chi_{R,ijk}^{(2)}\right| e^{i\delta} \tag{66}$$

where $|\chi_{R,ijk}^{(2)}|$ and $\delta(\omega_{IR})$ are the absolute magnitude and the phase (specifically, the phase change relative to the incident beam) of the resonant susceptibility, respectively. Polar co-ordinates are convenient to describe the susceptibility, as the magnitude and phase, plotted on an Argand diagram, can be directly related to experimental observations (53). The real vs. the imaginary component of the susceptibility is plotted as a function of the IR wavenumber on an Argand diagram (Fig. 10) for the situation represented in Fig. 9, i.e., an arbitrary resonance at $2900\,\text{cm}^{-1}$.

From Fig. 10 the origin of $|\chi_{R,ijk}^{(2)}|$ and $\delta(\omega_{IR})$ may be demonstrated by plotting the magnitude [Fig. 11(a)] and phase [Fig. 11(b)] vs. wavenumber.
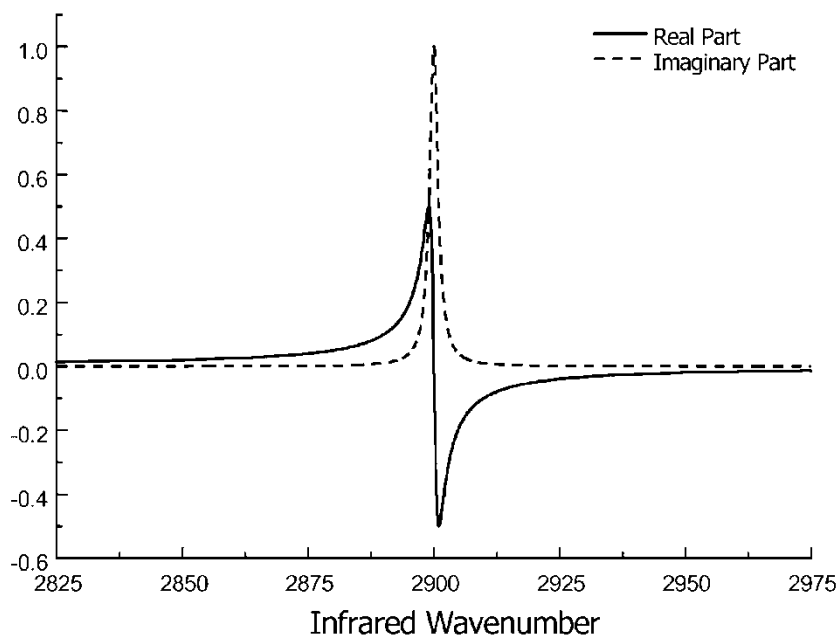

Figure 9. The real and imaginary components of $\chi_{R,ijk}^{(2)}$ for an arbitrary resonance at $2900\,\text{cm}^{-1}$. The damping constant, Γ, has been arbitrarily set to a value of 1.
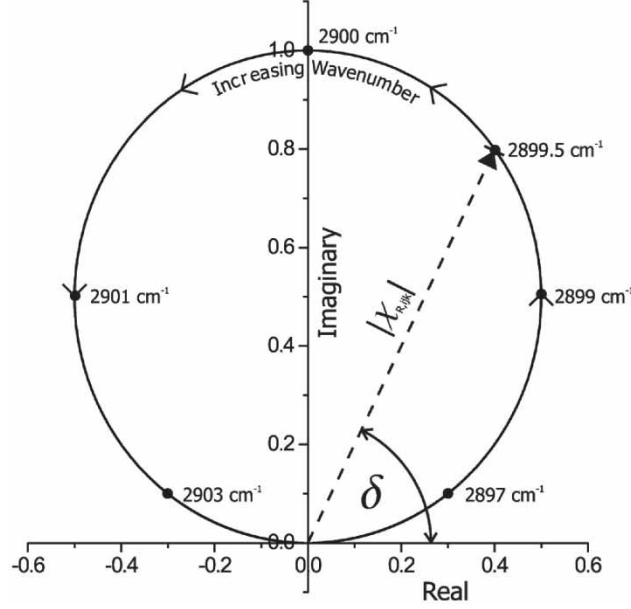
Figure 10. An Argand diagram demonstrating the origin of $|\chi_{R,ijk}^{(2)}|$ and $\delta(\omega_{IR})$. The real component of $\chi_{R,ijk}^{(2)}$ (from Fig. 9) is plotted on the x axis and the imaginary component (from Fig. 9) is plotted on the y axis, again arbitrarily set to a maximum Γ value of 1. A majority of the points lie on $(0, 0)$, but as the wavenumber increases a circle is traced out across the axes.

Non-resonant Susceptibility, $\chi_{NR,ijk}^{(2)}$

The non-resonant susceptibility has a magnitude and phase relationship with the incident beams that does not change significantly within the infrared wavenumber range considered here and is experimentally determined. The phase largely depends upon the properties of the metal, the frequency of the pump beam, and the nature of the surface plasmon resonance. For two commonly employed metals, gold and silver, the non-resonant phase is usually reported in the literature as $\pi/2$ and $\approx -\pi/4$, respectively, for a pump beam of wavelength 532 nm. With a fixed magnitude and phase relationship, the Argand diagram for a non-resonant susceptibility is trivial, as depicted in Fig. 12. In polar co-ordinates, $\chi_{NR,\;ijk}^{(2)}$ may be expressed as:

$$\chi_{NR,ijk}^{(2)} = \left|\chi_{NR,ijk}^{(2)}\right| e^{i\varepsilon} \tag{67}$$

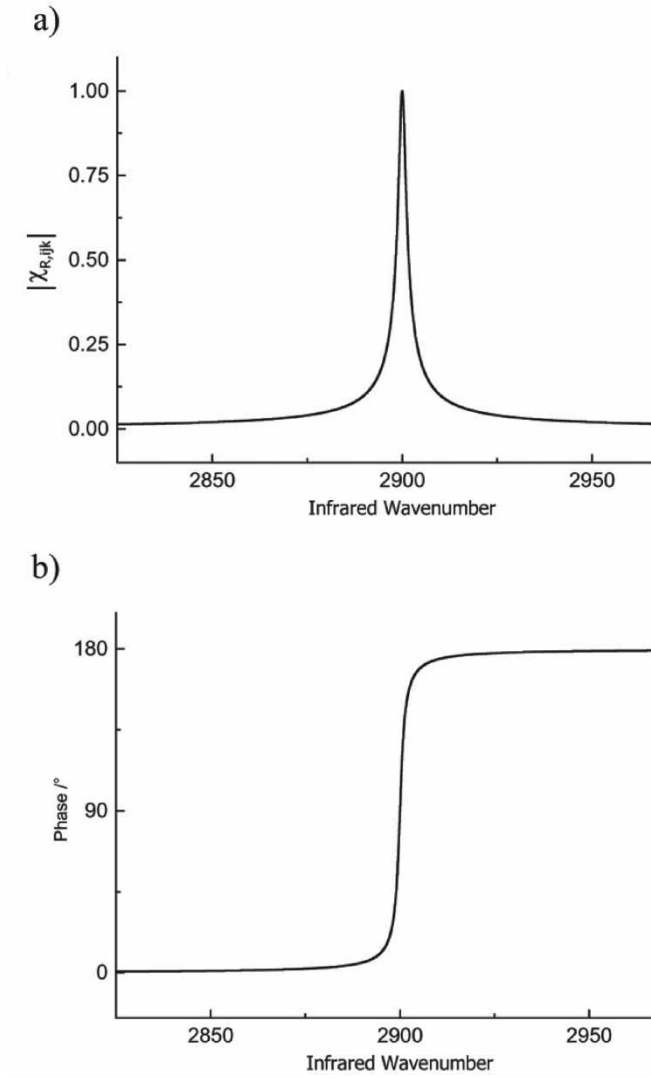where ε is the fixed, non-resonant phase of the substrate.

a)

b)

Figure 11. (a) The magnitude of $|\chi^{(2)}_{R,ijk}|$ and (b) the phase $\delta(\omega_{IR})$ of $\chi^{(2)}_{R,ijk}$.

The overall susceptibility of the surface is the summation of the resonant and non-resonant terms, i.e.,

$$\chi^{(2)}_{ijk} = \left|\chi^{(2)}_{R,ijk}\right|e^{i\delta} + \left|\chi^{(2)}_{NR,\ ijk}\right|e^{i\varepsilon} \tag{68}$$
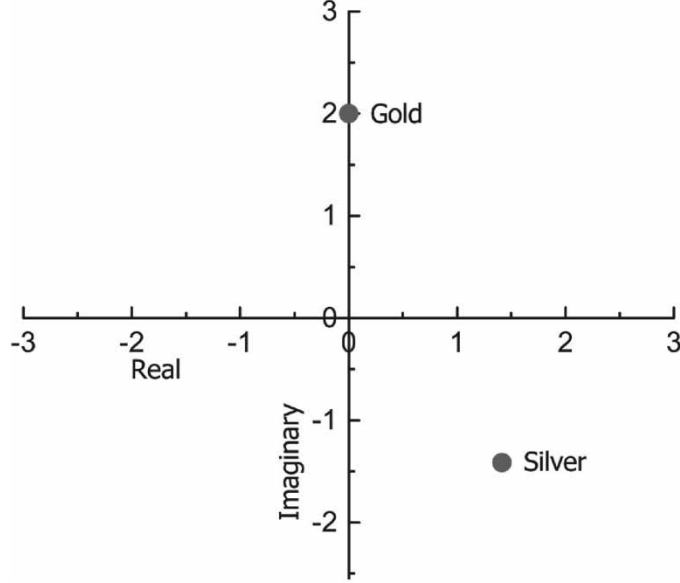
Figure 12. Non-resonant phase and magnitude for gold and silver substrates. An arbitrary non-resonant magnitude of 2 has been used to illustrate the two phase angles.

To visualise the interaction between the resonant and the non-resonant terms, it is useful to consider only one generic non-zero component of the susceptibility. The intensity of the SF light emitted from the surface may then be expressed as:

$$I_{SF} \propto \left| \left| \chi_{R,ijk}^{(2)} \right| e^{i\delta} + \left| \chi_{NR,ijk}^{(2)} \right| e^{i\varepsilon} \right|^2 \tag{69}$$

Consider an adsorbed monolayer on a dielectric substance, such as silica. In this instance, $|\chi_{NR,ijk}^{(2)}| \approx 0$, and consequently, the spectrum obtained is purely that of the resonant susceptibility [Fig. 13(a)]. For the same monolayer adsorbed on gold, the large non-resonant signal and the squared term in the intensity equation [Eq. (69)] results in significant amplification of the resonant signal [Fig. 13(b)]. Non-resonant amplification also occurs on silver, but as the non-resonant phase is $\approx -\pi/4$, it results in a more differential peak shape [Fig. 13(c)].

The Argand diagrams of Fig. 13 provide a visual interpretation of the resonant and non-resonant susceptibility effects; however, a mathematical
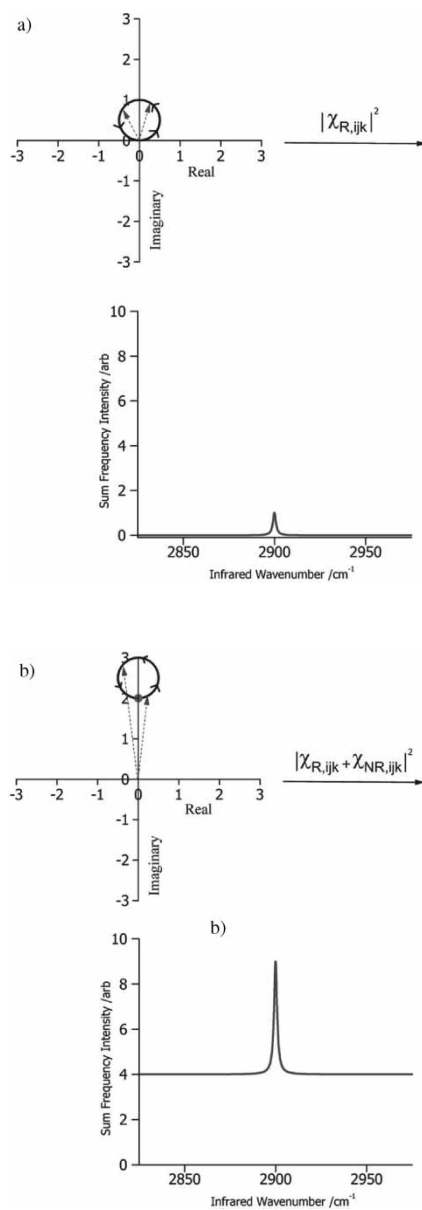
Figure 13. Argand diagrams and calculated SF spectra from monolayers on (a) silica, $|\chi^{(2)}_{NR,ijk}| \approx 0$, (b) gold, $|\chi^{(2)}_{NR,ijk}| \neq 0$, $\varepsilon = 90°$ and (c) silver $|\chi^{(2)}_{NR,ijk}| \neq 0$, $\varepsilon = -45°$. The spectra represent those obtained with the *ppp* laser beam polarisation combination and were generated using Eqs. (64) and (70), where $\omega_v = 2900\,\text{cm}^{-1}$, $\Gamma = 1$, $\varepsilon = 90°$ (b) and $\varepsilon = -45°$ (c). The magnitude of the non-resonant susceptibility was arbitrarily set at 2 for (b) and (c).
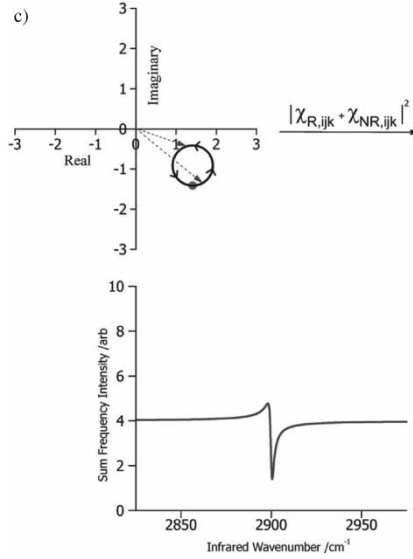
(continued)

Figure 13.   Continued.

description is also necessary. Equation (69) may be rewritten as:

$$I_{SF} \propto \left| \left| \chi^{(2)}_{R,ijk} \right| e^{i\delta} + \left| \chi^{(2)}_{NR,ijk} \right| e^{i\varepsilon} \right|^2$$

$$\propto \left| \left| \chi^{(2)}_{R,ijk} \right| e^{i\delta} + \left| \chi^{(2)}_{NR,ijk} \right| e^{i\varepsilon} \right| \cdot \left| \left| \chi^{(2)}_{R,ijk} \right| e^{-i\delta} + \left| \chi^{(2)}_{NR,ijk} \right| e^{-i\varepsilon} \right|$$

$$\propto \left| \chi^{(2)}_{R,ijk} \right|^2 + \left| \chi^{(2)}_{NR,ijk} \right|^2 + 2 \left| \chi^{(2)}_{R,ijk} \right| \left| \chi^{(2)}_{NR,ijk} \right| \cos[\varepsilon - \delta] \qquad (70)$$

The first two terms on the right-hand side of Eq. (70) are always positive, but the third (cross) term may be positive or negative. This cross term produces the resonant amplification and phase effects observed in Fig. 13 and it is the equation which provides the basis for modelling actual SF spectra. It should be noted that resonant line shapes may occur in many forms, dependent upon the substrate. It is, therefore, essential that they be modelled mathematically to determine intensities, phases, and vibrational band centres.

Probing Specific Resonant Susceptibility Components

The symmetry considerations presented earlier demonstrated that a surface with C_∞ symmetry has only seven $\chi^{(2)}_{ijk}$ components, which are non-zero:

$$\chi^{(2)}_{zxx}\left(=\chi^{(2)}_{zyy}\right) \quad \chi^{(2)}_{xzx}\left(=\chi^{(2)}_{yzy}\right) \quad \chi^{(2)}_{xxz}\left(=\chi^{(2)}_{yyz}\right) \quad \chi^{(2)}_{zzz}$$

Table 2. All possible polarisation combinations and the elements of $\chi_{ijk}^{(2)}$ that contribute to the spectrum

Polarisation combination	Elements of $\chi_{ijk}^{(2)}$
pss	$\chi_{zyy}^{(2)}$
sps	$\chi_{yzy}^{(2)}$
ss*p*	$\chi_{yyz}^{(2)}$
ppp	$\chi_{zzz}^{(2)}, \chi_{zxx}^{(2)}, \chi_{xzx}^{(2)}, \chi_{xxz}^{(2)}$

Note: The polarisations are listed in the order SF, visible, and infrared.

The p polarised light may be resolved into x and z components at the surface, whereas the s polarised light has a component solely in the y direction. With specific incident polarisation combinations, it is, therefore, possible to selectively probe particular susceptibilities. The polarisation of the emitted SF beam is determined purely from the non-zero $\chi_{ijk}^{(2)}$ components that generate the SF signal.

With dielectric surfaces such as silica, both s and p incident laser polarisations result in substantial surface **E** fields and all the combinations shown in Table 2 are, therefore, achievable. However, for metallic substrates, the reflectivity in the infrared wavelength region is often particularly high and it may be shown that the incident beam results in a large surface **E** field in the z directions, but negligible fields in the x and y direction (54). Thus, for a gold substrate, where over 97% of an incident infrared beam is reflected from the surface,[3] only resonant susceptibilities with a z infrared component generate a substantial SF signal, as listed in Table 3.

INTERPRETING SUM FREQUENCY SPECTRA

Vibrational Resonances

Three features of SF spectra, namely, the position, intensity, and phases of the vibrational resonances, provide information regarding the interfacial molecules. Although many vibrational resonances may be probed, those with strong infrared and Raman transition moments yield the most intense

---

[3]From Eq. (23), with an incident beam angle of 65° and refractive indices of air $= 1$ and gold $= 1.98 + 20.65I$, the Fresnel reflection coefficient, r_p, is 0.95 with a 12° phase change on reflection. Note that for reflection of an s polarised beam, the Fresnel reflection coefficient is -0.99, and a complete phase reversal therefore occurs.

Table 3. The limited polarisation combinations available for SFS on gold substrates

Polarisation combination	Elements of $\chi^{(2)}_{ijk}$
ssp	$\chi^{(2)}_{yyz}$
ppp	$\chi^{(2)}_{zzz}$, $\chi^{(2)}_{xxz}$

spectra [as evident from Eq. (57)]. Consequently, a large portion of the work reported in the literature has centred on probing the C−H vibrational modes (which have very strong IR and Raman transitions) of hydrocarbon containing species. Owing to the prevalence of this system, it will be used here as a representative model for analysis of spectra, although it should be borne in mind that the same principles may be applied to the interpretation of other molecular resonances.

The assignment of C−H vibrational modes observed by SFS is achieved by comparison with infrared and Raman spectra of alkanes (55), a summary of the assignments is given in Table 4. The terminal methyl group of an aliphatic hydrocarbon chain gives rise to three vibrational modes, depicted in Fig. 14. The symmetric stretching mode is split by Fermi resonance with an overtone of a methyl symmetric bending mode, thereby producing two frequencies: a low frequency component labelled r^+ (2878 cm^{-1}) and a high frequency component, r^+_{FR} (2942 cm^{-1}). The anti-symmetric stretching mode, r^-, consists of in-plane and out-of-plane components (illustrated in Fig. 14, the plane is defined by the C−C bonds). The two components are usually unresolved in SF spectra and appear as a single resonance at 2966 cm^{-1}.

The methylene groups in an aliphatic hydrocarbon chain give rise to three vibrational modes. The symmetric methylene stretching mode is split by Fermi resonance with an overtone of a deformation mode, thereby giving rise to two resonances (d^+ and d^+_{FR}). The d^+ mode appears in SF spectra as a sharp band at 2852 cm^{-1}, whereas the d^+_{FR} mode occurs as a broad band stretching from $\sim$ 2890 to 2930 cm^{-1}. In principle, an anti-symmetric methylene stretching mode, d^- (Fig. 14), can contribute to SF spectra at $\approx$2915 cm^{-1}. However, this mode is likely to be only very weakly SF active, as the d^- mode is observed at different wavenumbers in linear IR and Raman spectra (55).

Interfacial Conformation

The most highly ordered conformation of an alkyl chain is with its constituent carbon atoms lying in the same plane, which is a fully trans conformation. If a

Table 4. Resonant assignments and wavenumbers for C–H stretching modes observed by SF

Mode	Description	Wavenumber (cm^{-1})	
		In air (54,65)	In water (65)
r^+	Symmetric CH_3 stretch	2878	2874
r_{FR}^+	Symmetric CH_3 stretch (Fermi resonance)	2942	2933
r^-	Anti-symmetric CH_3 stretch	2966	2962
d^+	Symmetric CH_2 stretch	2854	2846
d_{FR}^+	Symmetric CH_2 stretch (Fermi resonance)	2890–2930	2890–2930
d^-	Anti-symmetric CH_2 stretch	2915	2916

Note: Slight frequency shifts are observed between adsorbed molecules studied in air and those studied under water. This shift is largely attributed to the changing polarity of the hydrocarbon environment (54).

single C–C bond were rotated by $120°$ a gauche defect would be formed and the carbons atoms would no longer all lie in the same plane. The hydrocarbon chain occupies a considerably larger volume when such a defect is introduced.

In an all-trans conformation, the majority of methylene groups lie in a locally centrosymmetric environment. By the rule of mutual exclusion, SF generation is forbidden [Eq. (57)] and hence both d^+ and d_{FR}^+ modes are SF inactive. The SF spectrum originating from a well-packed monolayer of an all-trans hydrocarbon chain, therefore, contains solely r^+, r_{FR}^+, and r^- resonances from the chain terminating methyl groups, as shown in Fig. 15(a). The energy difference between gauche and trans conformations ($\sim3.3\,kJ\,mol^{-1}$) is $\sim kT$ at room temperature. Thus, in a low density hydrocarbon monolayer, the alkyl chains may twist and flex with bonds adopting both trans and gauche conformations. Some gauche defects are more likely than others. Molecular dynamic simulations (56) and infrared spectroscopy measurements (57, 58) indicate that a gauche defect in the middle of a chain is more likely to occur when another gauche defect exists in the same chain. This gauche–trans–gauche conformation is known as a kink and can occur at relatively high surface densities, as the overall increase in volume of the hydrocarbon chain is limited. Note that a kink is a symmetrical defect and is, therefore, SF inactive. Isolated gauche defects generally occur towards the end of a hydrocarbon chain, where they do not significantly increase the surface area occupied by the adsorbed molecule. An isolated gauche defect breaks the symmetry of the hydrocarbon chain and results in SF active d^+ and d_{FR}^+
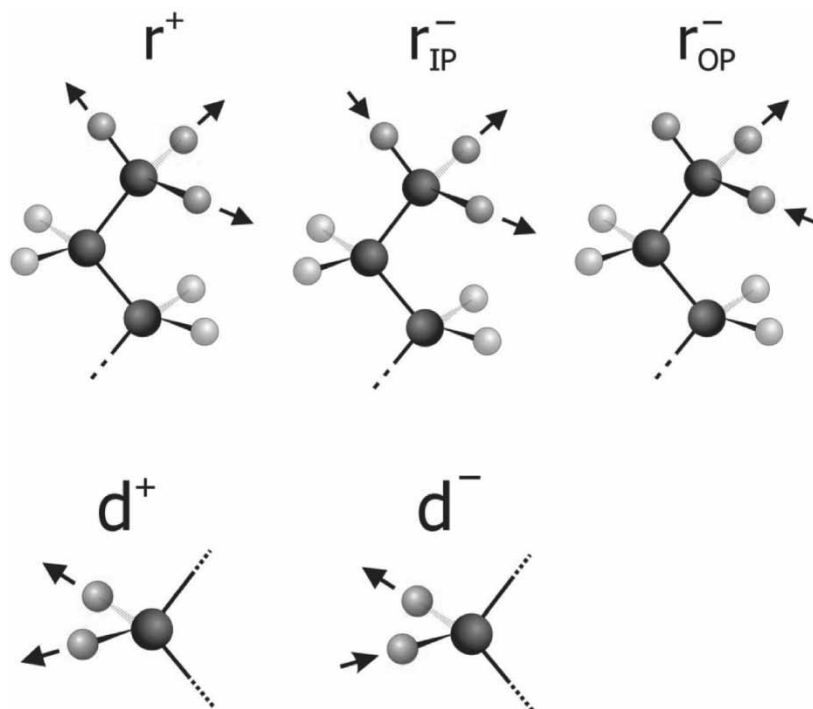
Figure 14. Methyl and methylene stretching modes. The internal displacement vectors of each vibrational mode are indicated by arrows (64). An in-depth symmetry analysis of the terminal methyl group of a long chain hydrocarbon is given in Ref. (51). IP, in-plane; OP, out-of-plane, where the plane is defined by the carbon–carbon bonds. For clarity, only the displacement of the hydrogen atoms is shown.

resonances. A second consequence of a gauche defect toward the end of an alkyl chain is that the neighbouring methyl group is tilted towards the surface, thereby decreasing its SF signal (see what follows). The SF spectrum from a monolayer containing isolated gauche defects is illustrated schematically in Fig. 15(b). At lower hydrocarbon surface densities, the proportion of isolated gauche defects increases, and initially the d^+ and d^+_{FR} resonance strengths increase, whereas the corresponding r^+ signal decreases [Fig. 15(c)]. If the interfacial hydrocarbon disorder increases further, the alkyl chains begin to assume an essentially random conformation on the surface, and the strengths of all resonances decrease in intensity due to orientational averaging [Fig. 15(d)]. At the limit of total disorder, the interfacial conformation is essentially random and all resonances are SF inactive. Figure 15 demonstrates that it is possible to examine an SF spectrum and qualitatively infer the general conformational order of interfacial molecules by inspection.
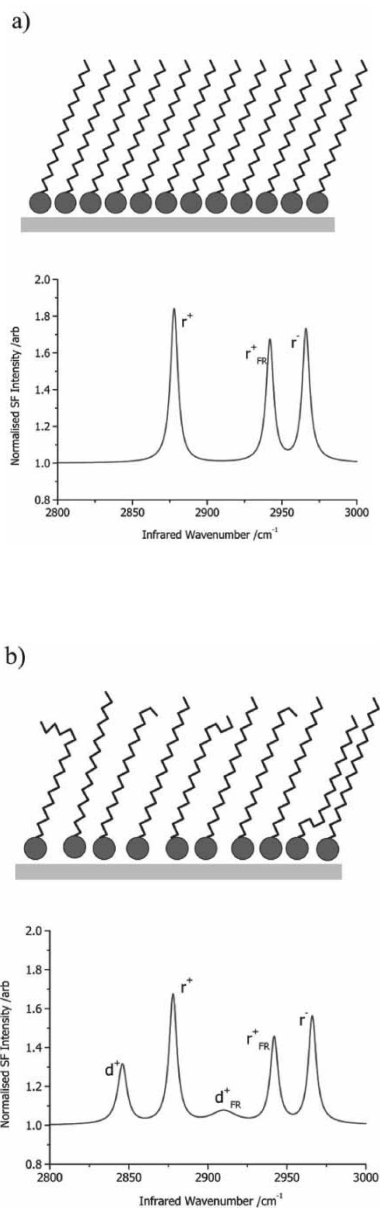
Figure 15. A representation of the effect of increased surface disorder on an SF spectrum. Surface disorder increases from (a) to (d). The depictions of the surface conformations and the simulated spectra are only intended to illustrate the qualitative trends that occur in a *ppp* SF spectrum with increasing disorder in the surface species.
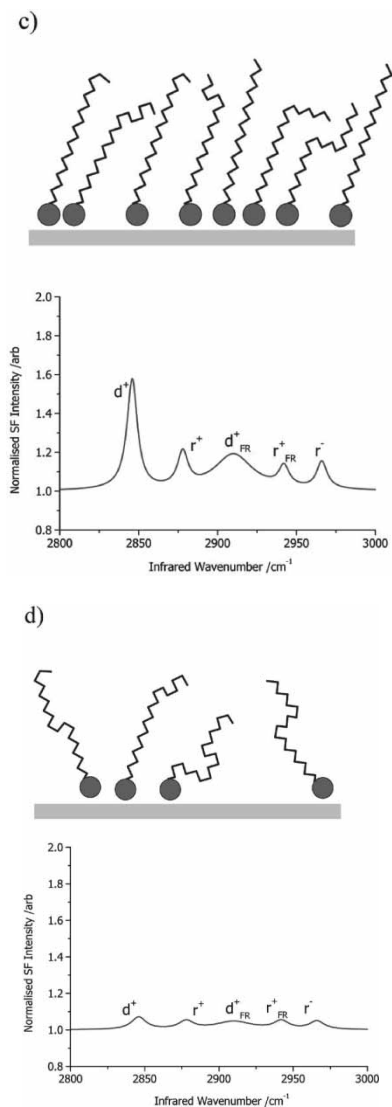
(continued)

c)

d)

Figure 15. Continued.

General Polar Orientation

The hydrocarbon chains of the amphiphilic molecules depicted in Fig. 15 extend away from their polar headgroups (depicted by the spherical terminus) in a generally positive z direction (away from the interface). For an isotropic surface (C_∞ symmetry), $z \neq -z$. Hence, if the molecules in

Fig. 15 were rotated by $180°$ to extend in the negative z direction, all the resonant susceptibilities would change sign (Table 5). When $\chi^{(2)}_{R,ijk}$ changes sign, both its real and imaginary components reverse sign and the phase circle plotted on an Argand diagram [Fig. 16(a)] is now traced in the opposite direction to earlier (Fig. 10) and lies in the negative-half of the imaginary axis. Furthermore, although a switch in molecular polar orientation does not change the magnitude of the resonant susceptibility, the phase is offset by $180°$, so that instead of varying from $0°$ to $180°$ through a resonance (for a positive $\chi^{(2)}_{R,ijk}$, Fig. 11), it varies from $180°$ to $360°$.

If molecules are present on a dielectric substrate ($\chi^{(2)}_{NR} = 0$) then the SF signal depends purely on $\chi^{(2)}_{R}$. A reversal in polar orientation, therefore, only produces a net-phase offset for the overall SF signal generated from the surface. This phase offset does not affect the intensity of the SF light and is, therefore, undetectable. To determine polar orientation from a dielectric substrate, the resonant SF signal from the surface must be combined with an external SF signal of known phase (59). This procedure is experimentally complex and is not performed routinely in SFS. However, if molecules are present on a surface with a significant non-resonant susceptibility ($\chi^{(2)}_{NR} \neq 0$), then a change in overall polar orientation is relatively easy to determine. If the orientation of the molecule is reversed, then the phase offset of $180°$ to δ in Eq. (70) reverses the sign of the cross-term, resulting in an overall change in the intensity of the SF signal, as illustrated in Fig. 16(b).

Molecular Tilt Angle to the Surface Normal

SFS may be used to determine the average orientation of molecules adsorbed at an interface. First, the independent contributing components of $\beta_{\alpha\beta\gamma}$ are identified from consideration of the molecular symmetry. Second, the

Table 5. The change in sign of resonant susceptibilities with reversal of molecular direction

$\chi^{(2)}_{R,zxx}$	$\chi^{(2)}_{R,-zxx} \equiv -\chi^{(2)}_{R,zxx}$
$\chi^{(2)}_{R,xzx}$	$\chi^{(2)}_{R,x-zx} \equiv -\chi^{(2)}_{R,xzx}$
$\chi^{(2)}_{R,xxz}$	$\chi^{(2)}_{R,xx-z} \equiv -\chi^{(2)}_{R,xxz}$
$\chi^{(2)}_{R,zzz}$	$\chi^{(2)}_{R,-z-z-z} \equiv \chi^{(2)}_{R,-zzz} \equiv -\chi^{(2)}_{R,zzz}$

hyperpolarisability is transformed from molecular to surface bound co-ordinates. This allows the $\beta_{\alpha\beta\gamma}$ components of a particular vibrational mode and functional group to be calculated for an individual $\chi^{(2)}_{R,ijk}$ component. For example, employing the methods and nomenclature outlined in detail in Refs. (25, 51), the contributing $\beta_{\alpha\beta\gamma}$ component of $\chi^{(2)}_{R,xxz}$ for r^+ is:

$$\langle \beta_{xxz} \rangle = \frac{\beta_{ccc}}{8}[\langle \cos \theta \rangle (1 + 7r) + \langle \cos 3\theta \rangle (r - 1)] \tag{71}$$
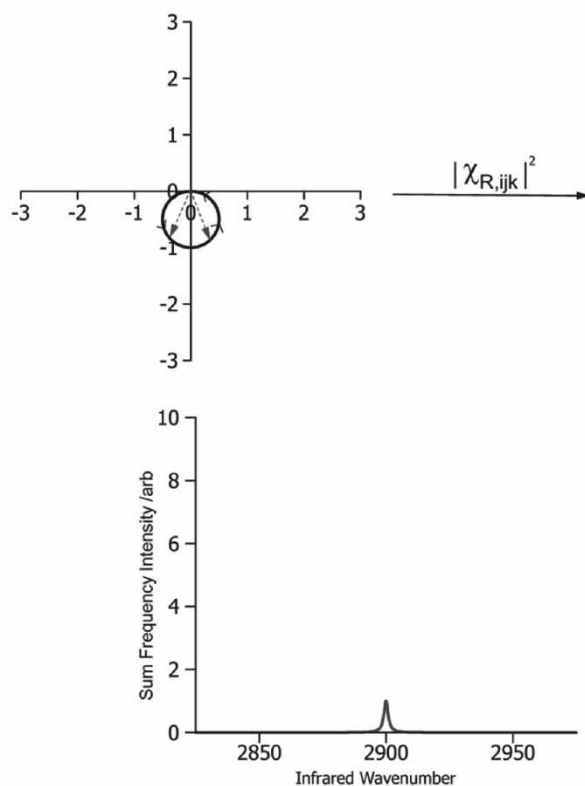

a)

Figure 16. Argand diagrams and simulated *ppp* SF spectra for molecules adsorbed with hydrocarbon chains oriented towards the surface. (a) Dielectric surface, $\chi^{(2)}_{NR} = 0$, the intensity of the SF light is simply related to the square of the resonant susceptibility. The change in phase of the susceptibility with orientation reversal has no observable effect. (b) Gold surface, $\chi^{(2)}_{NR} \neq 0$, the intensity of the SF light depends on the relationship between the resonant and the non-resonant susceptibilities [Eq. (70)]. The phase offset of the resonant susceptibility produces a spectral dip rather than a spectral peak as in Fig. 13(b).
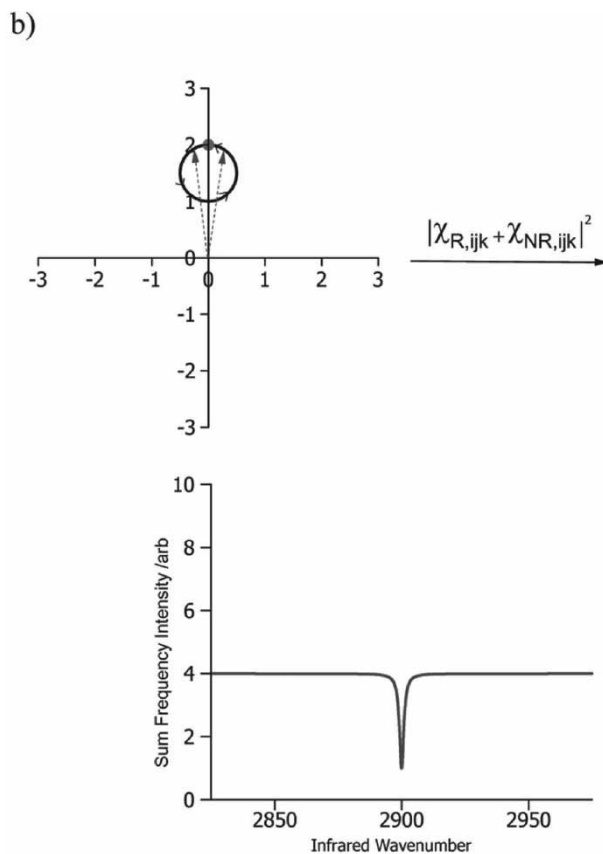
(continued)

b)

$$\xrightarrow{\quad |\chi_{R,ijk} + \chi_{NR,ijk}|^2 \quad}$$

Figure 16. Continued.

where θ is the angle of the molecular c axis to the surface normal and r is the ratio β_{aca}/β_{ccc}. For molecules adsorbed on a gold surface, the high reflectivity in the infrared region allows only a limited number of viable laser polarisation combinations, as described earlier and presented in Table 3. For the *ssp* and *ppp* laser polarisation combinations, the significant contributing susceptibility components are $\chi^{(2)}_{yyz}$ and $\chi^{(2)}_{zzz}$, $\chi^{(2)}_{xxz}$ respectively. To calculate the orientation of the methyl group, it is necessary to record SF spectra under both *ssp* and *ppp* polarisations, ensuring that the experimental variables of beam power, focus, and optical alignment remain as constant as possible. Modelling the un-normalised SF spectra provides a value for the strength of the vibrational mode, labelled $S_{ppp}(r^+)$ for an r^+ resonance probed with the *ppp* polarisation combination. The ratio between the strengths of the vibrational resonance can

then be related using Eq. (72).

$$\frac{S_{ssp}(r^+)}{S_{ppp}(r^+)} = \frac{L_{y,\text{SF}}K_{y,\text{VIS}}K_{z,\text{IR}}\langle\beta_{yyz}\rangle}{L_{x,\text{SF}}K_{x,\text{VIS}}K_{z,\text{IR}}\langle\beta_{xxz}\rangle + L_{z,\text{SF}}K_{z,\text{VIS}}K_{z,\text{IR}}\langle\beta_{zzz}\rangle} \tag{72}$$

where $\langle\beta_{yyz}\rangle = \langle\beta_{xxz}\rangle = (\beta_{ccc}/8)[\langle\cos\theta\rangle(1+7r) + \langle\cos 3\theta\rangle(r-1)]$ and $\langle\beta_{zzz}\rangle = (\beta_{ccc}/4)[\langle\cos\theta\rangle(3+r) - \langle\cos 3\theta\rangle(r-1)]$. Simplification allows the ratio of intensities to be related to purely r and θ. The ratio r may, in principle, be obtained from the Raman depolarisation ratio, ρ, and usually ranges from 1.66 to 3.5 (60, 61). The molecular orientation can subsequently be calculated by relating θ to κ, the orientation of the molecule to the surface normal (51).

The limited number of laser polarisation combinations possible on a metallic substrate, such as gold, increases the error in calculations of molecular tilt angles in comparison with calculations completed on dielectric surfaces, where all four laser polarization combinations may be employed (Table 2). Even with a dielectric substrate rather than a metal, the inherent inaccuracies in determining molecular tilt angle are considerable. Errors accrue in calculating resonant strengths (S) and SF Fresnel factors (L). However, the largest error normally arises from predicting the value of r, the ratio of β_{ccc} to β_{aac}. This value has a considerable effect on the results and can only be determined from Raman depolarization data or (rarely) by ab-initio calculations. Raman depolarization data is not always available for the chosen molecular entity, and the variation in assumed values of r often leads to large uncertainties in the calculated tilt angles.

MODELLING SUM FREQUENCY SPECTRA

The modelling of spectral data is an essential aspect of any SF experiment as it provides the frequency, strength, and width of the observed vibrational resonances, along with the strength and phase of any non-resonant signal. This information is crucial for accurate spectral interpretation and is fundamental to both conformational and orientational analysis. The mathematical models employed to analyse SF spectra are typically non-linear curve-fitting techniques which calculate the spectral characteristics of band centre, strength, and width, for any number of resonances within a spectrum.

As demonstrated earlier, the intensity of SF light emitted from an interface may be described in terms of the contributing resonant and non-resonant components [Eq. (70)]. If one considers a single non-zero generic susceptibility, it can be expressed as:

$$\begin{aligned} I_{\text{SF}} &\propto \left| \left|\chi_R^{(2)}\right|e^{i\delta} + \left|\chi_{NR}^{(2)}\right|e^{i\varepsilon} \right|^2 \\ &\propto \left|\chi_R^{(2)}\right|^2 + \left|\chi_{NR}^{(2)}\right|^2 + 2\left|\chi_R^{(2)}\right|\left|\chi_{NR}^{(2)}\right|\cos[\varepsilon - \delta] \end{aligned} \tag{73}$$

where δ and ε are the phases of the resonant and non-resonant terms, respectively. Equation (73) forms the basis of all spectral modelling calculations and is applicable to a single isolated resonance. Where two or more resonances are present in the spectrum, $\chi_R^{(2)}$ must be replaced by $\sum_v \chi_{R_v}^{(2)}$. Thus, for two resonances, Eq. (73) becomes:

$$I_{SF} \propto \left|\chi_{R_1}^{(2)}\right|^2 + \left|\chi_{R_2}^{(2)}\right|^2 + \left|\chi_{NR}^{(2)}\right|^2 + 2\left|\chi_{R_1}^{(2)}\right|\left|\chi_{NR}^{(2)}\right|\cos[\varepsilon - \delta_1]$$

$$+ 2\left|\chi_{R_2}^{(2)}\right|\left|\chi_{NR}^{(2)}\right|\cos[\varepsilon - \delta_2] + 2\left|\chi_{R_1}^{(2)}\right|\left|\chi_{R_2}^{(2)}\right|\cos[\delta_1 - \delta_2] \quad (74)$$

The magnitude and phase of the non-resonant susceptibility were described earlier and for a majority of spectral models are simply fitted to a single value and phase. The variation in published models usually occurs in the description of the resonant susceptibility. The simplest modelling technique is to describe the magnitude of the resonant susceptibility ($|\chi_R^{(2)}|$) in terms of a Lorentzian functional. However, the actual peak shape recorded by a spectrometer is dependant not only upon $|\chi_R^{(2)}|$, but also on experimental factors such as the line width of the laser beams (particularly for picosecond or femtosecond lasers). The SF spectral model, initially developed by Bain et al. (62) and now widely employed, incorporates a Lorentzian description of $|\chi_R^{(2)}|$, convoluted with a Gaussian distribution of vibrational frequencies, essentially creating a Gaussian distribution of Lorentzian lineshapes. The resulting combined function is similar to the Voigt profile used to model the lineshapes of high-resolution gas-phase infrared spectra of small molecules (63) which might contain pressure broadening (Lorentzian) and Doppler broadening (Gaussian) components. In order to demonstrate the principles of SF spectral modelling, however, the complexity of a combined Gaussian/Lorentzian or Voigt profile is not necessary and, consequently, a simple Lorentzian spectral model is developed as follows.

Lorentzian Spectral Model

A single general resonant susceptibility may be expressed as:

$$\chi_R^{(2)} = \frac{B}{(\omega_v - \omega_{IR} - i\Gamma)} \quad (75)$$

where the terms in the denominator have been defined in Eq. (57) and B is the strength of the vibrational mode and encompasses all contributing susceptibility and hyperpolarisability components as appropriate. Note that B is not the same as S employed in the previous section for the strength of a resonance, as S also accounts for Fresnel factor variations between different beam polarizations. The complete modelling equation [Eq. (73)] depends on the magnitude of the resonant susceptibility which may be calculated using

the relationship $|z| = \sqrt{(z \cdot \bar{z})}$, viz.,

$$\left|\chi_{\mathrm{R}}^{(2)}\right| = \sqrt{\frac{B}{(\omega_v - \omega_{\mathrm{IR}} - \mathrm{i}\Gamma)} \cdot \frac{B}{(\omega_v - \omega_{\mathrm{IR}} + \mathrm{i}\Gamma)}}$$

$$= \sqrt{\frac{B^2}{(\omega_v - \omega_{\mathrm{IR}})^2 + \Gamma^2}} \tag{76}$$

The peak height form of a Lorentzian line function is given by:

$$y = \frac{HW^2}{(\omega_v - \omega_{\mathrm{IR}})^2 + W^2} \tag{77}$$

where H is the peak height at $\omega_{\mathrm{IR}} = \omega_v$ and W is the half width at half the maximum height (HWHM). Comparison of Eqs. (76) and (77) reveals that the magnitude of the resonant susceptibility is related to the square root of the Lorentzian function:

$$\left|\chi_{\mathrm{R}}^{(2)}\right| = \sqrt{\frac{HW^2}{(\omega_v - \omega_{\mathrm{IR}})^2 + W^2}} \tag{78}$$

with $\Gamma = W$ and $B = \sqrt{(HW)}$. Hence Eq. (75) can be rewritten in terms of Lorentzian parameters:

$$\chi_{\mathrm{R}}^{(2)} = \frac{\sqrt{H}W}{(\omega_v - \omega_{\mathrm{IR}} - \mathrm{i}W)} \tag{79}$$

By separating Eq. (79) into its real and imaginary components [Eq. (65)], the phase of the generic susceptibility (δ) can be calculated trigonometrically from the Argand diagram:

$$\delta = \arctan\left(\frac{\mathrm{Im}\left[\chi_{\mathrm{R}}^{(2)}\right]}{\mathrm{Re}\left[\chi_{\mathrm{R}}^{(2)}\right]}\right) = \arctan\left(\frac{-W}{(\omega_v - \omega_{\mathrm{IR}})}\right) \tag{80}$$

For a single resonance, a least-squares fitting routine (e.g., the Levenberg–Marquardt method) would use Eqs. (73), (79), and (80) to generate the following equation:

$$I_{\mathrm{SF}} \propto \frac{HW^2}{(\omega_v - \omega_{\mathrm{IR}})^2 + W^2} + \left|\chi_{\mathrm{NR}}^{(2)}\right|^2 + 2\sqrt{\frac{HW^2}{(\omega_v - \omega_{\mathrm{IR}})^2 + W^2}}$$

$$\times \left|\chi_{\mathrm{NR}}^{(2)}\right| \cos\left[\varepsilon - \arctan\left(\frac{-W}{(\omega_v - \omega_{\mathrm{IR}})}\right)\right] \tag{81}$$

where both $|\chi_{\mathrm{NR}}^{(2)}|$ and its phase, ε, are fitted to single values that are invariant with frequency. The proportionality constant in Eq. (81) is difficult to

determine accurately, as it depends on the overlap integral between the electric fields of the two lasers, the linear and non-linear Fresnel factors, and the efficiency of the detector. The magnitude of the non-resonant signal does, however, provide an internal reference as for a given sample, the ratio $B/|\chi_{NR}|$ is independent of all instrumental factors and only the polarization and angle of incidence need to be fixed (62). SF spectral modelling is, therefore, completed with spectra normalised by the non-resonant background signal.

CONCLUSION

SFS is a powerful and increasingly commonly used technique for the elucidation of orientational and conformational information of interfacial species. This review is intended to aid those starting out in the field, or interested in the capabilities of the technique, to gain a fundamental understanding of this form of spectroscopy. This article has developed the theory of SFG from a tutorial viewpoint with the aim of demonstrating how the theory relates to the practical application of the technique and the analysis of the resulting spectra.

ACKNOWLEDGMENTS

REFERENCES

1. Bain, C.D. (1995) Sum-frequency vibrational spectroscopy of the solid–liquid interface. *J. Chem. Soc. Faraday Trans.*, 91: 1281–1296.
2. Shen, Y.R. (1989) Surface properties probed by second-harmonic and sum-frequency generation. *Nature*, 337: 519–525.
3. Adamson, A.W. and Gast, A.P. (1999) *Physical Chemistry of Surfaces*; John Wiley & Sons: New York, 1–808.
4. Bloembergen, N. and Pershan, P.S. (1962) Light waves at the boundary of nonlinear media. *Phys. Rev.*, 128: 606–622.
5. Bloembergen, N. (1999) Surface nonlinear optics: a historical overview. *Appl. Phys. B*, 68: 289–293.
6. Zhu, X.D., Suhr, H., and Shen, Y.R. (1987) Surface vibrational spectroscopy by infrared-visible sum frequency generation. *Phys. Rev. B Con. Mater.*, 35: 3047–3050.
7. Hunt, J.H., Guyot-Sionnest, P., and Shen, Y.R. (1987) Observation of C–H stretching vibrations of monolayers of molecules optical sum frequency generation. *Chem. Phys. Lett.*, 133: 189–192.

8. Harris, A.L., Chidsey, C.E.D., Levinos, N.J., and Loiacono, D.N. (1987) Monolayer vibrational spectroscopy by infrared-visible sum frequency generation at metal and semiconductor surfaces. *Chem. Phys. Lett.*, 141: 350–356.

9. Hess, C., Bonn, M., Funk, S., and Wolf, M. (2000) Hot-band excitation of CO chemisorbed on Ru(001) studied with broadband-IR sum-frequency generation. *Chem. Phys. Lett.*, 325: 139–145.

10. Dederichs, F., Friedrich, K.A., and Daum, W. (2000) Sum-frequency vibrational spectroscopy of CO adsorption on Pt(111) and Pt(110) electrode surfaces in perchloric acid solution: effects of thin-layer electrolytes in spectroelectrochemistry. *J. Phys. Chem. B*, 104: 6626–6632.

11. Baldelli, S., Markovic, N., Ross, P., Shen, Y.R., and Somorjai, G. (1999) Sum frequency generation of CO on (111) and polycrystalline platinum electrode surfaces: evidence for SFG invisible surface CO. *J. Phys. Chem. B*, 103: 8920–8925.

12. Hirose, C., Ishida, H., Iwatsu, K., Watanabe, N., Kubota, J., Wada, A., and Domen, K. (1998) In situ SFG spectroscopy of film growth. I. General formulation and the analysis of the signal observed during the deposition of formic acid on Pt(110)-(1 × 2) surface. *J. Chem. Phys.*, 108: 5948–5956.

13. Somorjai, G.A., Su, X.C., McCrea, K.R., and Rider, K.B. (1999) Molecular surface studies of adsorption and catalytic reaction on crystal (Pt, Rh) surfaces under high pressure conditions (atmospheres) using sum frequency generation (SFG)—surface vibrational spectroscopy and scanning tunneling microscopy (STM). *Topic Catalysis*, 8: 23–34.

14. Morita, A. and Hynes, J.T.A. (2000) Theoretical analysis of the sum frequency generation spectrum of the water surface. *Chem. Phys. Lett.*, 258: 371–390.

15. Shen, Y.R. (1998) Frank Isakson prize address sum frequency generation for vibrational spectroscopy: applications to water interfaces and films of water and ice. *Solid State Commun.*, 108: 399–406.

16. Schnitzer, C., Baldelli, S., and Shultz, M.J. (1999) Sum frequency generation by water on supercooled H_2SO_4/H_2O liquid solutions at stratospheric temperature. *Chem. Phys. Lett.*, 313: 416–420.

17. Schnitzer, C., Baldelli, S., and Shultz, M.J. (2000) Sum frequency generation of water on NaCl, $NaNO_3$, $KHSO_4$, HCl, HNO_3, and H_2SO_4 aqueous solutions. *J. Phys. Chem. B*, 104: 585–590.

18. Pizzolatto, R.L., Yang, Y.J., Wolf, L.K., and Messmer, M.C. (1999) Conformational aspects of model chromatographic surfaces studied by sum-frequency generation. *Anal. Chim. Acta.*, 397: 82–92.

19. Ebert, V., Schulz, C., Volpp, H.R., Wolfrum, J., and Monkhouse, P. (1999) Laser diagnostics of combustion processes: from chemical dynamics to technical devices. *Isr. J. Chem.*, 39: 1–24.

20. Berg, O. and Klenerman, D. (2003) Vibrational spectroscopy of mechanically compressed monolayers. *J. Am. Chem. Soc.*, 125: 5493–5500.

21. Beattie, D.A., Haydock, S., and Bain, C.D. (2000) A comparative study of confined organic monolayers by Raman scattering and sum-frequency spectroscopy. *Vib. Spectrosc.*, 24: 109–123.

22. Du, Q., Xiao, X., Charych, D., Wolf, F., Frantz, P., Shen, Y.R., and Salmeron, M. (1995) Nonlinear optical studies of monomolecular films under pressure. *Phys. Rev. B Con. Mater.*, 51: 7456–7463.

23. Ward, R.N., Duffy, D., Davies, P.B., and Bain, C.D. (1994) Sum-frequency spectroscopy of surfactants adsorbed at a flat hydrophobic surface. *J. Phys. Chem.*, 98: 8536–8542.

24. Ward, R.N., Davies, P.B., and Bain, C.D. (1997) Coadsorption of sodium dodecyl sulfate and dodecanol at a hydrophobic surface. *J. Phys. Chem. B*, 101: 1594–1601.

25. Bell, G.R., Bain, C.D., and Ward, R.N. (1996) Sum-frequency vibrational spectroscopy of soluble surfactants at the air–water interface. *J. Chem. Soc. Faraday Trans.*, 92: 515–524.

26. Braun, R., Casson, B.D., and Bain, C.D. (1995) A sum-frequency study of the two-dimensional phase transition in a monolayer of undecanol on water. *Chem. Phys. Lett.*, 245: 326–334.

27. Chen, Z., Ward, R., Tian, Y., Baldelli, S., Opdahl, A., Shen, Y.R., and Somorjai, G.A. (2000) Detection of hydrophobic end groups on polymer surfaces by sum-frequency generation vibrational spectroscopy. *J. Am. Chem. Soc.*, 122: 10615–10620.

28. Wei, X., Hong, S.C., Zhuang, X., Goto, T., and Shen, Y.R. (2000) Nonlinear optical studies of liquid crystal alignment on a rubbed polyvinyl alcohol surface. *Phys. Rev. E Stat. Phys. Plasmas Fluids Relat. Interdiscip. Topics*, 62: 5160–5172.

29. Smiley, B.L. and Richmond, G.L. (2000) Assembly of long chain phosphatidylcholines at a liquid–liquid interface. *Biopolymers*, 57: 117–125.

30. Walker, R.A., Gragson, D.E., and Richmond, G.L. (1999) Induced changes in solvent structure by phospholipid monolayer formation at a liquid–liquid interface. *Colloid Surface A*, 154: 175–185.

31. Lobau, J., Sass, M., Pohle, W., Selle, C., Koch, M.H.J., and Wolfrum, K. (1999) Chain fluidity and phase behaviour of phospholipids as revealed by FTIR and sum-frequency spectroscopy. *J. Mol. Struct.*, 481: 407–411.

32. Roke, S., Schins, J., Muller, M., and Bonn, M. (2003) Vibrational spectroscopic investigation of the phase diagram of a biomimetic lipid monolayer. *Phys. Rev. Letts.*, 90: 128101-1–128101-4.

33. Petralli-Mallow, T., Briggman, K.A., Richter, L.J., Stephenson, J.C., and Plant, A.L. (1999) Nonlinear optics as a detection scheme for biomimetic sensors: SFG spectroscopy of hybrid bilayer membrane formation. *Proc. SPIE*, 25: 1–7.

34. Wang, J., Buck, S.M., and Chen, Z. (2003) The effect of surface coverage on conformational changes of bovine serum albumin molecules at the air–solution interface detected by sum frequency generation vibrational spectroscopy. *Analyst*, 128: 773–778.

35. Kim, G., Gurau, M., Kim, J., and Cremer, P.S. (2002) Investigations of lysozyme adsorption at the air/water and quartz/water interfaces by vibrational sum frequency spectroscopy. *Langmuir*, 18: 2807–2811.

36. Wang, J., Buck, S.M., and Chen, Z. (2002) Sum frequency generation vibrational spectroscopy studies on protein adsorption. *J. Phys. Chem. B*, 106: 11666–11672.

37. Kim, J. and Somorjai, G.A. (2003) Molecular packing of lysozyme, fibrinogen, and bovine serum albumin on hydrophilic and hydrophobic surfaces studied by infrared-visible sum frequency generation and fluorescence microscopy. *J. Am. Chem. Soc.*, 125: 3150–3158.

38. Koffas, T.S., Kim, J., Lawrence, C.C., and Somorjai, G.A. (2003) Detection of immobilized protein on latex microspheres by IR-visible sum frequency generation and scanning force microscopy. *Langmuir*, 19: 3563–3566.

39. Wang, J., Buck, S.M., and Chen, Z. (2002) Molecular responses of proteins at different interfacial environments detected by sum frequency generation vibrational spectroscopy. *J. Am. Chem. Soc.*, 124: 13302–13305.
40. Miranda, P.B. and Shen, Y.R. (1999) Liquid interfaces: a study by sum-frequency vibrational spectroscopy. *J. Phys. Chem. B*, 103: 3292–3307.
41. Chen, Z., Shen, Y.R., and Somorjai, G.A. (2002) Studies of polymer surfaces by sum frequency generation vibrational spectroscopy. *Annu. Rev. Phys. Chem.*, 53: 437–465.
42. Williams, C.T. and Beattie, D.A. (2002) Probing buried interfaces with non-linear optical spectroscopy. *Surf. Sci.*, 500: 545–576.
43. Lorentz, H.A. (1952) *The Theory of Electrons*; Dover: New York.
44. Boyd, R.W. (1992) *Nonlinear Optics*; Academic Press: Sandiego, 148.
45. Casson, B.D. (1998) Phase transitions in surfactant monolayers. University of Oxford, Ph.D. Thesis.
46. Franken, P.A., Hill, A.E., Peters, C.W., and Weinreich, G. (1961) Generation of optical harmonics. *Phys. Rev. Lett.*, 7: 118–119.
47. Shen, Y.R. (1984) *The Principles of Nonlinear Optics*; Wiley: New York; Chaps. 6 and 25.
48. Heinz, T.F. (1982) Nonlinear optics of surfaces and adsorbates. University of California, Berkeley, Ph.D. Thesis, Appendix I.
49. Hirose, C., Akamatsu, N., and Domen, K. (1992) Formulas for the analysis of the surface SFG spectrum and transformation coefficients of cartesian SFG tensor components. *Appl. Spectr.*, 46: 1051–1072.
50. Hecht, E. (1987) *Optics*, 2nd Ed.; Addison–Wesley: Reading, Massachusetts.
51. Lambert, A.G. (2001) Resonantly enhanced sum frequency spectroscopy of adsorption on hydrophilic mica substrates, University of CambridgePh.D. Thesis.
52. Hunt, J.H., Guyot-Sionnest, P., and Shen, Y.R. (1987) Observation of C–H stretch vibrations of monolayers of molecules optical sum-frequency generation. *Chem. Phys. Lett.*, 133: 189–192.
53. Braun, R., Casson, B.D., Bain, C.D., van der Ham, E.W.M., Vrehen, Q.H.F., Eliel, E.R., Briggs, A.M., and Davies, P.B. (1999) Sum-frequency generation from thiophenol on silver in the mid and far-IR. *J. Chem. Phys.*, 110: 4634–4640.
54. Ward, R.N. (1993) Sum-frequency spectroscopy of molecules at interfaces. University of Cambridge, Ph.D. Thesis.
55. Macphail, R.A., Strauss, H.L., Snyder, R.G., and Elliger, C.A. (1984) Carbon–hydrogen stretching modes and the structure of *n*-alkyl chains. 2. Long, all-trans chains. *J. Phys. Chem.*, 88: 334–341.
56. Karaborni, S. and Toxvaerd, S. (1992) Molecular dynamics simulations of Langmuir monolayers: a study of structure and thermodynamics. *J. Chem. Phys.*, 96: 5505–5515.
57. Maroncelli, M., Strauss, H.L., and Snyder, R.G. (1985) The distribution of conformational disorder in the high-temperature phases of the crystalline *n*-alkanes. *J. Chem. Phys.*, 82: 2811–2824.
58. Kim, Y., Strauss, H.L., and Snyder, R.G. (1989) Conformational disorder in crystalline *n*-alkanes prior to melting. *J. Phys. Chem.*, 93: 7520–7526.
59. Superfine, R., Huang, J.Y., and Shen, Y.R. (1990) Phase measurement for surface infrared-visible sum-frequency generation. *Opt. Lett.*, 15: 1276–1278.
60. Zhuang, X., Miranda, P.B., Kim, D., and Shen, Y.R. (1999) Mapping molecular orientation and conformation by surface nonlinear optics. *Phys. Rev. B*, 59: 12632–12640.

61. Wolfrum, K. and Laubereau, A. (1994) Vibrational sum-frequency spectroscopy of an adsorbed monolayer of hexadecanol on water. Destructive interference of adjacent lines. *Chem. Phys. Lett.*, 228: 83–88.
62. Bain, C.D., Davies, P.B., Ong, T.H., and Ward, R.N. (1991) Quantitative analysis of monolayer composition by sum-frequency vibrational spectroscopy. *Langmuir*, 7: 1563–1566.
63. Gadzuk, J.W. and Luntz, A.C. (1984) On vibrational lineshapes of adsorbed molecules. *Surf. Sci.*, 144: 429–450.
64. Wilson, E.B., Decius, J.C., and Cross, P.C. (1955) *Molecular Vibrations*; McGraw-Hill: New York; Chaps. 3 and 4.
65. Macphail, R.A., Synder, R.G., and Strauss, H.L. (1982) The motional collapse of the methyl C–H stretching vibration bands. *J. Chem. Phys.*, 77: 1118–1137.